REVIEW

Check for updates

Recent developments of lead-free halide double perovskites: a new superstar in the optoelectronic field

Sukanya Ghosh, Hari Shankar and Prasenjit Kar [ID] *

Metal halide perovskites have come to the limelight in the field of optoelectronic devices in the last few decades. Owing to their unique optical and electronic properties along with variable morphologies, perovskite materials have attracted widespread attention compared to conventional semiconductors. The power conversion efficiency of perovskites has reached beyond 25% in the last few years. Besides solar cell application, perovskite materials are explored towards light emitting diodes, sensors, photoconductors and other electrochemical applications. Unfortunately, the toxicity and instability issues render the large-scale commercial application of halide perovskite despite having excellent characteristics with flexibility for optoelectronic applications. The scientific community is searching for lead-free non-toxic and stable perovskites to overcome this problem. Especially double perovskites have gained importance in this purpose due to their similar characteristics to lead halide perovskites. Moreover, double perovskites exhibit interesting optical and morphological properties. In this review we discuss the different aspects of double perovskites in detail.

1. Introduction

In the history of human civilization, the demand for energy has never been stronger. The growing population and increasing worldwide quality of living have put a strain on the world's finite energy supplies.[1,2] The human energy consumption has increased dramatically in the past 150 years, from 5×10^{12} kW h per year to 1.2×10^{14} kW h per year. While the world's population has grown by a factor of four in the past century, the energy demand has grown by a factor of twenty-four. Hydrocarbons such as oil and gas account for more than 80% of this energy. This reality makes access to fossil fuels more challenging, and the environmental consequences of their use necessitate the development of natural, sustainable alternative energy sources. Solar energy, wind energy, hydroelectricity, biofuels, geothermal energy, hydrogen energy, ocean energy, and biomass energy are only a few of them.[3–5] Governments and concerned citizens are attempting to prioritize the use of renewable resources and reduce the reckless use of natural resources through increased conservation. Perovskite materials demonstrate that they can be used as alternative energy sources. Metal halide perovskites have been vastly studied and reported in the last few years.[6]

1.1. Birth and character of perovskites

The origin of perovskite materials is based on the discovery of Calcium Titanium Oxide ($CaTiO_3$). In 1839, Russian scientist

Department of Chemistry, Indian Institute of Technology Roorkee, Uttarakhand-247667, India. E-mail: kar.prasen@gmail.com, prasenjit.kar@cy.iitr.ac.in

Count Lev Alekseyevich von Perovski first discovered the structure of $CaTiO_3$.[7] Thereafter, any material having a similar structure to $CaTiO_3$ is known as a perovskite material. The most commonly studied halide perovskites have the general formula ABX_3. Here A is a monovalent metal cation (MA^+, CS^+, FA^+), B is a divalent metal cation (Pb^{2+}), and X is a halide ion (Cl^-, Br^-, I^-).[8] The crystal structure of an ideal cubic perovskite represents the B atom in the center of the lattice surrounded by octahedron anions. A is located at interstices which are surrounded by eight octahedra in the cuboctahedral gap. The overall structure looks like a three dimensional network.[9] Kojima *et al.* first reported metal halide hybrid perovskite $MAPbI_3$ in 2009.[10] 3D halide perovskite materials have been widely studied due to their outstanding properties. Excellent characteristics such as high light absorption coefficients, low temperature solution processing capability, narrow band emission, direct bandgaps, long exciton diffusion lengths, suitable charge carrier lifetimes, high photoluminescence quantum yields (PLQY) and low nonradiative carrier recombination rates[11–14] make perovskite materials attractive in the field of optoelectronic devices.

1.2. Structural considerations

The general structure of perovskite materials is like the structure of $CaTiO_3$. Depending on the size of cations and anions, perovskite materials have different crystal structures. The stability and formability of an ideal perovskite having the general formula ABX_3 mainly depend on three factors: (1) charge

neutrality between cations and anions,[15] (2) stability of BX_6 octahedra, which meets the requirement of the octahedral factor (μ),[16,17] and (3) the Goldschmidt tolerance factor (t)[18] related to the size of cations and anions. The octahedral factor is evaluated by using the radii of cation B and anion X.

$$\mu = r_B/r_X$$

The value of the octahedral factor for a stable perovskite material is between 0.442 and 0.895.[19]

The Goldschmidt tolerance factor (t) can be calculated by the radii of cations A and B and anion X.[20]
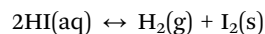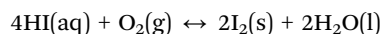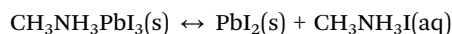
$$t = r_A + r_X/\sqrt{2}(r_B + r_X)$$

The tolerance factor varies in the range of 0.8 to 1.0 for perovskite materials based on the cationic and anionic sizes. The empirical tolerance factor values for stable and pure perovskite materials are found to be: $0.8 \leq t \leq 1.0$.[16] Materials with a tolerance factor of 1.0 can form perfect cubic crystal structures (Fig. 1a).[21]

If the value of the tolerance factor is less than 0.8, then the size of cation A is too small to fit in the lattice. On the other hand, if $t > 1.0$, the size of cation A is too big to form a perfect perovskite structure. In that case, the concept of the formation of a hexagonal structure arises.[16,22,23] Cubic crystal structures predominate for perovskite materials when the tolerance factor lies between 0.9 and 1.0. If t is 0.8–0.9 then orthorhombic, rhombohedral and tetragonal (Fig. 1b and c) perovskite crystals are more prone to form.

1.3. Advantages and disadvantages of halide perovskites

The power conversion efficiency of halide perovskites has increased enormously within the last few years. In 2009 the power conversion efficiency was 3.8%, which has increased up to 25% in recent years.[24,25] Therefore, metal halide perovskites have gained intense attention as promising alternatives to conventional semiconductor materials for next generation optoelectronic applications with a facile synthesis process.[26] In addition to solar cells,[28] halide perovskites can be successfully applied to light emitting diodes (LEDs),[27] photodetectors,[29] lasers,[30] field effect transistors (FETs),[31] radiation detectors,[32] encryption devices,[33] *etc.* Perovskite materials are now a hot topic in the optoelectronic field. The chemical stability of perovskites yet enables their outdoor

application.[34a] Lead halide perovskites are susceptible to ready degradation in the presence of moisture, sunlight and UV radiation.[34b,35] Degradation occurs in the following ways:[36]

$$CH_3NH_3PbI_3(s) \leftrightarrow PbI_2(s) + CH_3NH_3I(aq)$$

$$CH_3NH_3I(aq) \leftrightarrow CH_3NH_2(aq) + HI(aq)$$

$$4HI(aq) + O_2(g) \leftrightarrow 2I_2(s) + 2H_2O(l)$$

$$2HI(aq) \leftrightarrow H_2(g) + I_2(s)$$

Likewise, water reacts with metal hybrid perovskites to form $((CH_3NH_3)_4PbX_6 \cdot 2H_2O)$ which may weaken the hydrogen bonding interaction between the organic cation of the A site and the inorganic PbX_6 octahedron of the B site. By this way, the crystal structure of the perovskite lattice changes.[37] In this regard, $MAPbBr_3$ is more stable than $MAPbI_3$ as moisture can penetrate easily[38] into $MAPbI_3$ due to the difference of ionic radius (Table 1). $MAPbI_3$ is prone to decompose more readily at a humidity of $>55\%$ compared to $MAPbBr_3$ under the same conditions.[38] Degradation in the presence of moisture, sunlight and oxygen causes a low efficiency[39] of perovskites by the decrease of fluorescence intensity and photoluminescence quantum yields, which has poor impact on their photovoltaic application.

The toxicity of lead is another concern for the commercialization and large scale application of halide perovskites. Lead is a potent toxin for the environment and human body (Fig. 2).[40a] Even at a low exposure limit, it can cause severe damage to the nervous system and renal system, and also leads to impaired bone calcification.[40b] The ability of lead to replace the Ca^{2+} ion in protein kinase C enzyme affects the nervous system.[41] Lead poisoning primarily arises by the ability of lead to form covalent bonds with the active site of the thiol group of many enzymes, which inhibits the activity of many antioxidant enzymes.[42] Lead can easily contaminate environmental systems due to the water solubility of PbI_2 (the K_{sp} value for PbI_2 is 9.8×10^{-9} at $25\,^{\circ}C$).[43] This is the common problem for any toxic metal ion which is water soluble, mainly in polar solvents, and can be extracted into the environment easily through water.[44] Lead can damage the ecosystems in the environment as well as in our body by this mechanism. In order to overcome these problems, researchers are trying to replace lead ions in the perovskite family with other homovalent and heterovalent cations, which results in more stable and less toxic perovskite materials. We will discuss this briefly in the next section.

1.4. Formability of lead-free perovskites

Oxide perovskites have attracted considerable attention due to their excellent magnetic properties such as paramagnetism, ferromagnetism and magnetoresistance power.[45–52] Halide perovskites have impressed the scientific community by their aforementioned properties (mentioned in Section 1.1) which are very interesting for potential photovoltaic application. However, the toxicity of lead and instability in the presence of moisture, sunlight and humid conditions are responsible for
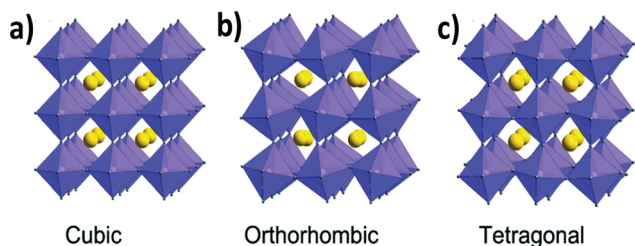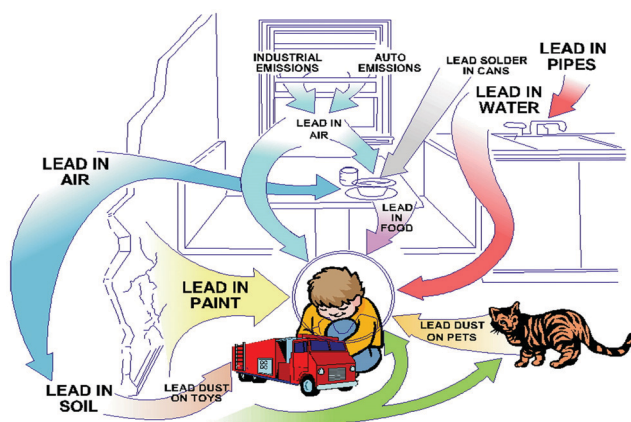

Fig. 1 Different crystal structures of metal halide perovskites: (a) cubic, (b) orthorhombic and (c) tetragonal. Reproduced with permission.[26] Copyright 2019, Royal Society of Chemistry.

Table 1 Ionic radii of ions in different sites of the perovskite lattice

Cation (A)	Effective radius (Å)	Ref.	Cation (B)	Effective radius (Å)	Ref.	Anion (X)	Effective radius (Å)	Ref.
Methylammonium $[(CH_3)NH_3]^+$	2.17	23	Pb^{2+}	1.19	53	Chloride (Cl^-)	1.81	55
Formamidinium $[CH(NH_2)_2]^+$	2.53	23	Sn^{2+}	1.10	54	Bromide (Br^-)	1.96	55
Cs^+	1.88	53	Sn^{4+}	0.69	53	Iodide (I^-)	2.20	55
K^+	1.64	53	Ca^{2+}	1.00	53			
Rb^+	1.72	53	Ge^{2+}	0.73	53			
			Mg^{2+}	0.72	53			
			Sr^{2+}	1.18	53			
			Ba^{2+}	1.35	53			
			Cu^{2+}	0.73	53			
			Fe^{2+}	0.78	53			
			Pd^{2+}	0.86	53			
			Bi^{3+}	1.03	53			
			Sb^{3+}	0.76	53			
			Ag^+	1.29	53			

Fig. 2 Exposure of the environment and children to lead. Reproduced with permission.[40a] Copyright 2018, Taylor & Francis.

the non-commercialization and non industrialization of lead halide perovskite materials. Therefore, researchers are trying to find alternatives to lead based perovskites and develop lead-free halide perovskites for large scale application and capitalization. In Table 1 we summarise some commonly used metal ions in the lattice sites of A, B and X and their corresponding ionic radii which are important factors for the successful formation of perovskite materials.

1.5. Design of lead-free perovskites

Regarding the toxicity of lead, replacement of lead ions with other homovalent metal cations[56] having similar electronic configurations is a great approach. In this respect, tin and germanium can be potential alternatives as they belong from the same group in the periodic table. However, their poor stability in the divalent states hinders them from forming ideal 3D perovskite lattice structures. These materials are less stable as compared to their lead analogues. Due to the inert pair effect, the +2 states of tin and germanium are less stable than the corresponding +4 oxidation states, having a negative impact on their photovoltaic applications.[57] A wide range of metal ions such as Ca, Pd, Cd, Hg, Ba, Be, Pt, Ni, Co, Zn, Mn, Fe, and Sr

with stable divalent oxidation states can be considered as replacements for lead. However, all metal ions are not environmentally friendly (Cd, Hg) and suitable for photovoltaic application because of their high band gap (Be, Ca, Ba, Sr). Considering all the facts, Co, Ni, Mn, and Zn are the most promising candidates.[58,59]

The heterovalent substitution of lead can give rise to 3D, 2D and 0D layered perovskites (Fig. 3b and c). Lead can be replaced by tetravalent metal cations (B^{4+}) such as Sn^{4+} and Pd^{4+}, leading to the formation of A_2BX_6 type perovskites.[60a,b] In addition to that, two trivalent metal cations (Bi^{3+}, Sb^{3+}) may also replace three lead ions to produce layered $A_3B_2X_9$ compounds (Fig. 3b and d). Recently, research on double perovskites has gained tremendous importance due to their higher stability and non-toxic nature as compared to lead halide perovskites. The replacement of two divalent lead ions with heterovalent cations, i.e. one trivalent and one monovalent cations, leads to the formation of double perovskites. Double perovskites have
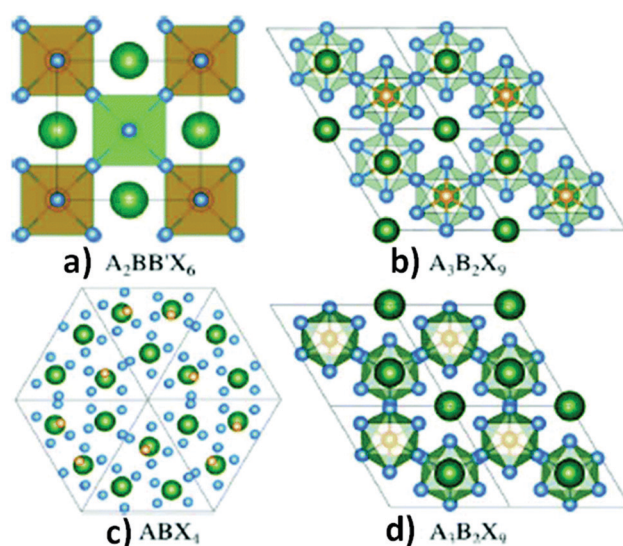

Fig. 3 (a) Double perovskites, (b) 2-D perovskites, (c) 0-D perovskites and (d) polymorphs. Reproduced with permission.[61] Copyright 2017, American Chemical Society.

the general formula of $A_2BB'X_6$ (Fig. 3a), where B is a monovalent cation (Ag^+, Cu^+) and B' is a trivalent metal ion (Bi^{3+}, In^{3+}, Sb^{3+}). Two toxic divalent lead ions are replaced by non-toxic monovalent (B) and trivalent (B') metal ions in double perovskites which neutralize the overall charge in the perovskite lattice like conventional perovskites.[60c–g] Double perovskites are named so because their unit cell is double that of lead halide perovskites. Among all the possible structures of lead-free perovskites, double perovskites have come to the limelight due to their considerable stability and optoelectronic properties, which opens up a new avenue in the field of optoelectronic applications.

Unlike lead halide perovskites, very few review articles have been published on lead-free halide double perovskites about their synthesis, characterization and applications. Sargent *et al.* reported the development of the structures and stability of double perovskites.[61] Liao *et al.* addressed the progress of lead-free perovskites.[62] Tesfemichale *et al.* published an article which covered the electronic and optical properties of lead-free hybrid perovskites for optoelectronic applications.[63] Inorganic layered and lead-free perovskites have been focused on for various photovoltaic applications such as LEDs, lasers, and solar cells.[64] Nag *et al.* successfully highlighted the future aspects of Cs_2AgBiX_6 double perovskite nanocrystals.[65] Numerous studies have been done to enhance the stability and tune the band gap.[61] Recent theoretical and experimental approaches on the optical, electronic and defect properties of perovskite materials have been discussed in the report of Xiao *et al.*.[66] Fan *et al.* focused on the synthesis and properties of lead-free perovskite quantum dots.[67]

In this review, our aim is to present a complete picture of double perovskite (Scheme 1) materials which include both microcrystals and nanocrystals (Scheme 3). Earlier we discussed how double perovskite materials have gained importance (Scheme 2) and its significant factors. The probability for the formation of different structures of double perovskites was considered in the previous section. Later we are going to discuss deliberately the synthetic process of double perovskites. This review covers various optoelectronic properties of double perovskites. We have also aimed to discuss their different morphologies and stability. Finally, the optoelectronic application of double perovskites is investigated here. Among all the
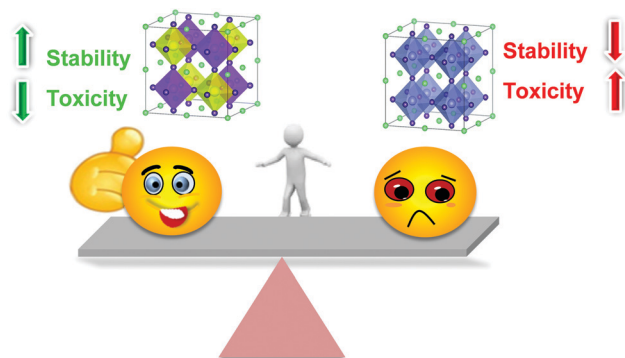
Scheme 2   Differences between lead-free double perovskites and lead halide perovskites.

possible formations of double perovskite materials, Cs_2AgBiX_6 has been explored vastly. Besides it, $Cs_2AgInCl_6$, $Cs_2AgSbCl_6$, and $Cs_2CuSbCl_6$ have also gained attention due to their considerable properties.

# 2. Material synthesis and crystal structures of halide double perovskites

Metal halide double perovskite materials like lead halide perovskites can be synthesized by a variety of ways such as spin coating, mechanochemical, anti-solvent reprecipitation, hot injection, and solvothermal methods.

2.1.   Synthesis and crystal structures of double perovskite microcrystals

Organic–inorganic hybrid double perovskites were first reported in 2016. The Anthony K. Cheetham group reported MA_2KBiCl_6.[68] They first synthesized the starting material CH_3NH_3Cl by mixing CH_3NH_2 and HCl at 273 K temperature and then heating the mixture to 323 K for drying. MA_2KBiCl_6 was crystallized by mixing MACl, KCl and $BiCl_3$ at 423 K in HCl medium by the hydrothermal technique. The resulting MA_2KBiCl_6 double perovskite crystallised in $R\bar{3}m$ symmetry. The
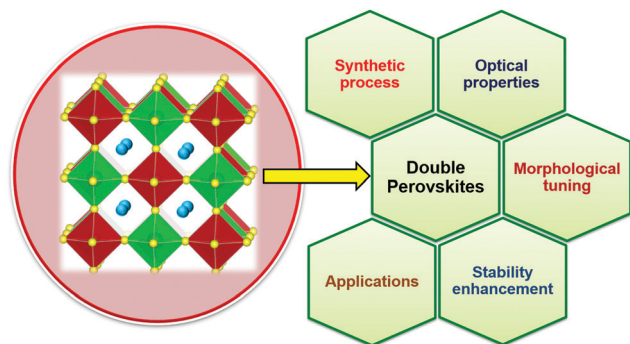
Scheme 1   Schematic representation of lead-free double perovskites and distinct features of double perovskites discussed in the review.
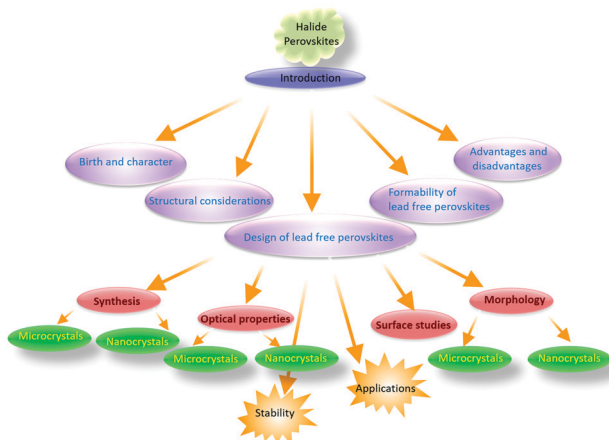
Scheme 3   Summary of the review.

authors compared the experimentally observed crystal structure with the density functional theory (DFT) model. The K–Cl bond length was slightly distorted and had a value of 3.049 Å. Bi–Cl had a bond distance of 2.681 Å. The K–Cl–Bi bridging angle was 173.04°. Wei *et al.* reported $MA_2AgBiBr_6$ 3D cubic double perovskite,[69] which crystallized in the $Fm\bar{3}m$ space group having a lattice parameter of 11.64 Å. The Ag–Br and Bi–Br bond lengths were 2.95 and 2.87 Å respectively. Deng *et al.* reported $MA_2TiBiBr_6$ which is isoelectronic with $MAPbBr_3$.[70] This was also crystallized in a 3D cubic structure with the space group $Fm\bar{3}m$ and had a lattice parameter of 11.76 Å. Yin *et al.* established theoretical calculation by the DFT model for synthesis of various chalcogenide double perovskites.[71] The frozen-core projected augmented wave approach was used here including the core and electron applications. The authors identified nine chalcogenide double perovskites. These are Sr_2SbTaS_6, Ba_2SbTaS_6, Sr_2BiNbS_6, Ba_2BiNbS_6, Sr_2BiTaS_6, Ba_2BiTaS_6, Ba_2SbTaS_6, Ba_2BiNbS_6, and $Ba_2BiTaSe_6$. Slavney *et al.* reported a $Cs_2AgBiBr_6$ double perovskite single crystal.[72] The large orange-red single crystal was synthesized from a concentrated HBr solution containing stoichiometric amounts of CsBr, AgBr and $BiBr_3$. The single crystal showed a cubic face with space group $Fm\bar{3}m$ having a unit cell of 11.25 Å. Cubic $Cs_2AgBiBr_6$ (Fig. 4a)[73] with space group $Fm\bar{3}m$ was also reported by the spin coating approach in 2018. CsBr, AgBr, and $BiBr_3$ were mixed in a molar ratio of 2:1:1 in dimethyl sulfoxide to form a supersaturated solution. Before spin coating, both the precursor and substrate were preheated at 80 °C. Giustino *et al.* reported a series of lead-free double perovskite materials.[74] DFT calculations for all the materials have been reported where $Cs_2AgBiCl_6$ double perovskite was synthesized only. Single phase $Cs_2AgBiCl_6$ was prepared by a solid state reaction procedure in a sealed fused silica ampoule. The starting materials CsCl, AgCl and $BiCl_3$ were mixed in a ratio of 2:1:1 and were loaded into the sealed silica ampoule under a vacuum of 10^{-3} Torr. The mixture was heated to 500 °C for five hours and held at 500 °C for four hours. Finally, upon cooling to room temperature, a yellow polycrystalline product was obtained. The authors also performed structural refinement by the single crystal

X-ray diffraction technique. Woodward *et al.* synthesized two lead-free double perovskites, $Cs_2AgBiCl_6$ and $Cs_2AgBiBr_6$.[75] Double perovskites have been synthesized *via* both the solid state and solution phase synthetic procedures. Polycrystalline Cs_2AgBiX_6 was prepared from a mixture of HCl or HBr solution. H_3PO_2 and metal halide salts were also used during the synthesis. The collected precipitate was washed with ethanol and dried overnight. The authors also developed a way to synthesize $Cs_2Ag-BiX_6$ polycrystalline samples by mixing all the halide salts in a solid state synthesis process. All the reagents were ground for 20 minutes and then kept in a box furnace in air at 210 °C for 10 hours. It was found that two heating cycles were needed with grinding in between to obtain the phase pure products. All the compounds obtained from all of the synthetic routes showed similar X-ray diffraction (XRD) patterns. Double perovskites were crystallized in the cubic phase with space group $Fm\bar{3}m$. Our group recently reported an interesting phenomenon to synthesize $Cs_2Ag-BiX_6$ (X = Cl, Br) microcrystals in organic medium and a mixture of aqueous and organic media.[76] All the halide salts were dissolved in DMSO to form the precursor. Then the precursor was injected into isopropanol to obtain the desired products in the organic medium. For the synthesis of materials in aqueous–organic media, we first dissolved bismuth halides in water in one pot and then concentrated acid was added to it to dissolve it completely. In another pot, cesium and silver halides were dissolved in DMSO and then all the halides were mixed together.

100 µL precursor was injected into the isopropanol followed by oleic acid to obtain the desired products. Both the reactions were carried out at 80 °C. We noticed that there was no change in the crystal structures of the microcrystals synthesized in the different media. All the materials were crystallized in their cubic face with space group $Fm\bar{3}m$. Angshuman Nag *et al.* reported the synthesis of $Cs_2AgInCl_6$ microcrystals and their corresponding Yb doped analogue.[77] Microcrystals were synthesized from HCl medium by stoichiometrically mixing all halide salts. In order to synthesize the Yb doped double perovskites, the authors mixed $YbCl_3$, $InCl_3$ and AgCl in a sample vial containing HCl and heated the mixture at 75 °C under vigorous
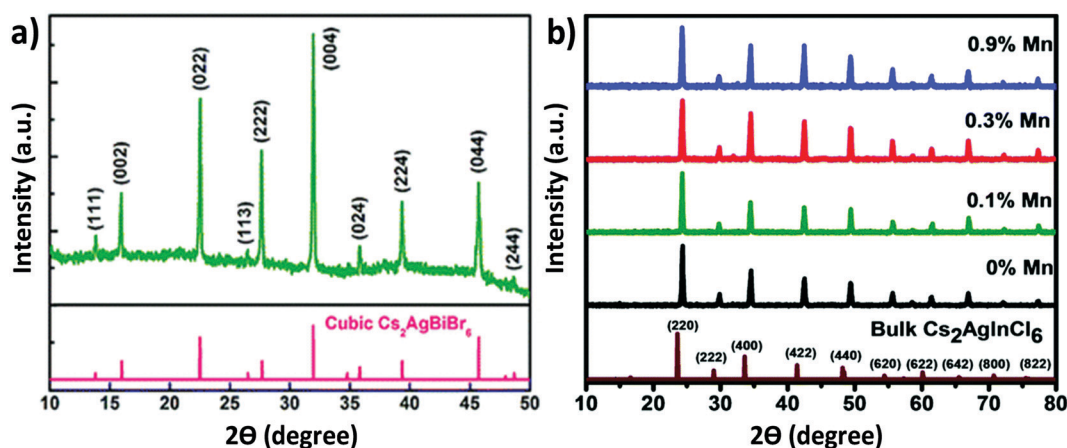

Fig. 4 XRD pattern of (a) the $Cs_2AgBiBr_6$ thin film. Reproduced with permission.[73] Copyright 2018, Royal Society of Chemistry. XRD patterns of (b) undoped and Mn doped $Cs_2AgInCl_6$ double perovskite MCs. Reproduced with permission.[78] Copyright 2018, Royal Society of Chemistry.

stirring. After 20 minutes, CsCl was added to the solution. Then the reaction mixture was filtered and the precipitate was dried at 110 °C in an oven. Nag et al. also reported Mn doped $Cs_2AgInCl_6$.[78] Mn doped $Cs_2AgInCl_6$ was also synthesized by a similar procedure like Yb doped $Cs_2AgInCl_6$. All the undoped and doped compounds were crystallized in their cubic phase double perovskite with space group $Fm\bar{3}m$. It was noticed that there was no significant change in the crystal structure upon doping $MnCl_2$ in the $Cs_2AgInCl_6$ double perovskite material (Fig. 4b). This was attributed to the small dopant concentration of $MnCl_2$ in the parent perovskite. Crystal growth of $Cs_2AgInCl_6$ is also possible by the hydrothermal process.[79] Liu et al. synthesized a $Cs_2AgInCl_6$ microcrystal by the hydrothermal method in a stainless steel Parr autoclave using 0.5 mL HCl, 2.4 mmol CsCl, 1.2 mmol AgCl and 1.2 mmol $InCl_3$.[79] They observed that white powder was obtained when the reaction was carried out at 423 K for 12 hours. At 423 K temperature, a large crystal was also formed by the continuation of the reaction for 72 hours. The product was filtered out and washed in ethanol and dried overnight for material characterization. The authors found that the $Cs_2AgInCl_6$ octahedral crystal formed by the alternation of $AgCl_6$ and $InCl_6$ in all three directions, which finally formed a 3D network. Synthesis of Cu doped double perovskites has a great impact on their optoelectronic properties.[80a,b]

Michaelis et al. synthesized $Cs_2AgSbCl_6$ and Cu doped $Cs_2AgSbCl_6$ double perovskites via solvent based synthesis.[80a] Here AgCl was prepared by mixing $AgNO_3$ and HCl. At first 10 M HCl and H_3PO_2 were mixed and then heated to 120 °C. Then Sb_2O_3, AgCl and CsCl were added to it which finally formed a pale yellow colour precipitate. Cu doped analogues were synthesized using a similar process by the addition of different amounts of $CuCl_2$ during the reaction. The XRD patterns showed that a face centred cubic double perovskite was formed with space group $Fm\bar{3}m$ and a lattice parameter of 10.699 Å. The authors found that incorporation of Cu ions into the perovskite lattice resulted in a decrease of lattice parameter as the XRD plane shifted toward higher 2θ values (Fig. 5a) and the area (Fig. 5b) along with full width half maximum (FWHM) of the peak increased (Fig. 5c). This occurred due to the lower ionic radius of the dopant Cu^{2+} (0.87 Å) ion than those of Ag^+ (1.29 Å) and Sb^{3+} (0.90 Å). Another antimony based lead-free Cs_2CuSbX_6 (X = Cl, Br) was proposed theoretically.[74] George Volonakis reported $Cs_2AgInCl_6$ double perovskite[81] by optimizing the structures of perovskite materials within the local density approximation (LDA) to DFT. A face centred cubic phase with an $Fm\bar{3}m$ elpasolite unit cell was used as a structural template in that calculation. The atomic model consisted of InX_6 and AgX_6 octahedra which alternate along the (100), (010) and (001) directions. The obtained lattice constants for Cl, Br and I were 10.20 Å, 10.74 Å and 11.52 Å respectively. Volonakis et al. proposed that it is possible to synthesis Cl, Br and mixed Cl/Br analogues of Cs_2AgInX_6 experimentally and not the I derivative through the calculation of the tolerance factor and octahedral factor. However, $Cs_2AgInCl_6$ was synthesized by the solution based method at 110 °C using 10 M HCl, CsCl, AgCl, and $InCl_3$ salts.
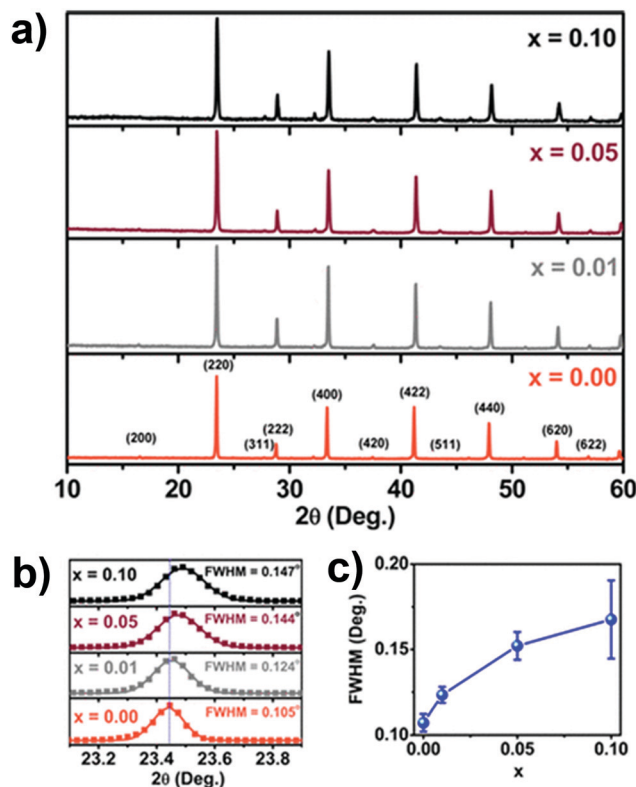

Fig. 5 (a) XRD patterns of undoped and Cu doped $Cs_2AgSbCl_6$ MCs, (b) expansion of the (220) plane in the XRD patterns and (c) broadening of the FWHM. Reproduced with permission.[80a] Copyright 2018, American Chemical Society.

2.2. Synthesis and crystal structures of double perovskite nanocrystals

Double perovskite nanocrystals can be synthesized by a variety of processes like double perovskite microcrystals.

The Keli Han group synthesized Cs_2AgBiX_6 double perovskite nanocrystals by a solution based procedure.[82] The authors dissolved all the halide salts in DMSO medium. Then they injected the precursor solution into an anti-solvent, isopropanol, in the presence of surface ligand oleic acid to form the desired nanocrystals. The nanocrystals were crystallized in the cubic phase with space group $Fm\bar{3}m$. Alivisatos et al. reported two lead-free double perovskite nanocrystals $Cs_2AgInCl_6$ and $Cs_2AgSbCl_6$.[83] They developed a different synthetic process (Fig. 6a) for crystal growth. During the synthesis of $Cs_2AgInCl_6$ they used benzoyl chloride, whereas 2-ethyl-2-hexonyl chloride was used for the synthesis of $Cs_2AgSbCl_6$. Acetate salts of all metal ions were mixed in xylene at the time of synthesis of $Cs_2AgInCl_6$. Then oleic acid, oleylamine and benzoyl chloride were added to it and the reaction mixture was heated to 100 °C. After it, the resulting mixture was centrifuged and redispersed into hexane for material characterization. Acetate salts, oleic acid, oleylamine, xylene and 2-ethyl-2-hexonyl chloride were used for the synthesis of $Cs_2AgSbCl_6$ via a hot injection method. Both the nanocrystals exhibited a cubic phase with the $Fm\bar{3}m$ space group in the XRD pattern. The authors also carried out spin-polarized PBE-GGA based DFT for structural relaxation.
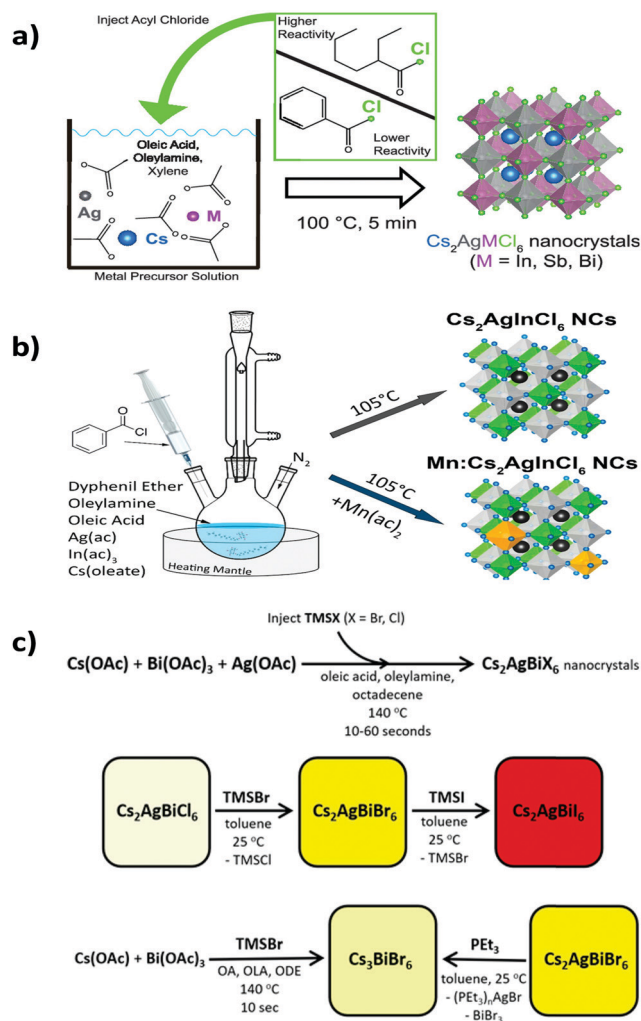
Fig. 6 Synthesis of (a) metal halide double perovskite nanocrystals. Reproduced with permission.[83] Copyright 2019, American Chemical Society. Synthesis of (b) undoped and Mn doped $Cs_2AgInCl_6$ nanocrystals. Reproduced with permission.[84] Copyright 2018, American Chemical Society. (c) Cs_2AgBiX_6 nanocrystals *via* an anion exchange method. Reproduced with permission.[86] Copyright 2018, American Chemical Society.

Nag *et al.* reported Yb doped $Cs_2AgInCl_6$ double perovskite nanocrystals.[77] Here also acetate salts of silver, indium and benzoyl chloride were used and the reaction was carried out *via* a hot injection method like the previously mentioned process. Nag *et al.* used cesium oleate as a precursor. Cesium oleate was prepared by mixing cesium carbonate and oleic acid at 140 °C and it was preheated to 100 °C before using in a reaction. A nitrate salt of Yb was used as a Yb precursor for doping Yb ions into the parent $Cs_2AgInCl_6$ nanocrystals. It was observed that due to the small dopant Yb concentration, there was no significant shift in 2θ value in the XRD peak positions. L. Manna *et al.* reported undoped and Mn doped $Cs_2AgInCl_6$ nanocrystals *via* a hot injection method.[84] Silver acetate, indium acetate, cesium oleate, diphenyl ether (DPE), oleylamine and benzyl ether were used for the synthesis of nanocrystals (Fig. 6b). Mn was doped into the nanocrystals by using manganese acetate precursor. Keli Han *et al.* also reported the

synthesis of Mn doped double perovskite nanocrystals.[85] In this case the mother material was $Cs_2NaIn_xBi_{1-x}Cl_6$. The nanocrystals were synthesized by a variable temperature and one pot hot injection method. In the hot injection method, acetate salts of cesium, sodium, bismuth and indium were loaded into a mixture of oleic acid, oleylamine and octadecene, which was heated for 60 minutes under vacuum at 110 °C. Manganese acetate was added into the stirring reaction mixture to synthesise Mn doped nanocrystals. The nanocrystals revealed the cubic face centred structure with the $Fm\bar{3}m$ space group in the X-ray diffraction pattern. There is a monotonic shift of diffraction peaks towards higher 2θ values in the powder XRD profile with the increase of the In/Bi ratio. This happens due to the smaller ionic radius of In^{3+} (94 ppm) than Bi^{3+} (117 ppm). Chlorine and bromine halide double perovskites have been explored vastly over iodine based double perovskites. Multiple computational studies have been done on the Cs_2AgBiI_6 double perovskite as a target of interest. However, experimentally it is difficult to synthesise due to its readily decomposable nature. Computational studies have been performed to investigate whether the material is thermodynamically stable with respect to its decomposition into another phase. In addition to that, Gamelin *et al.* reported an outstanding synthetic route for Cs_2AgBiI_6 *via* a halide exchange procedure (Fig. 6c).[86] Gamelin *et al.* synthesized Cs_2AgBiX_6 double perovskite nanocrystals by a hot injection method. They also reported that postsynthetic modification through anion exchange and cation extraction can give rise to Cs_2AgBiI_6, which is difficult to synthesise by any conventional process. Cesium acetate, silver acetate and bismuth acetate were mixed in octadecene, oleic acid and oleylamine to synthesize the nanocrystals. Then TMSCl was added to it to form $Cs_2AgBiCl_6$ nanocrystals. TMSCl was swiftly injected at 160 °C. Then centrifugation of the reaction mixture at 9000 rpm for 20 minutes followed by centrifugation at 10 000 rpm and 6000 rpm by dissolving it in toluene and hexane, respectively, resulted in the formation of the desired nanocrystals, whereas addition of TMSBr formed $Cs_2AgBiBr_6$ nanocrystals. It was also demonstrated that the Br congener can be synthesized from the Cl congener by the addition of TMSBr to the $Cs_2AgBiCl_6$ nanocrystals. Similarly, addition of TMSI to the $Cs_2AgBiBr_6$ nanocrystals results in Cs_2AgBiI_6 double perovskite nanocrystals. Individually $Cs_2AgBiCl_6$ and $Cs_2AgInCl_6$ have gained attention in various synthetic approaches. In this respect, Bi doped $Cs_2AgInCl_6$ nanocrystals were also reported in the literature.[87] Pristine and Bi doped $Cs_2AgInCl_6$ have been synthesized *via* a hot injection method. Powder XRD of these materials revealed the highly crystalline nature of the nanocrystals with space group $Fm3m$.

In Table 2 we summarize the various synthetic approaches with the respective space groups obtained from the XRD patterns for different lead-free double perovskite microcrystals (MCs) and nanocrystals (NCs).

3. Optical properties

The optical properties of lead-free halide double perovskites are obtained from their visible light harvesting properties. The

Table 2 Synthetic processes and space groups of double perovskites

Material	Synthesis process	Space group	Ref.
MA_2KBiCl_6 MC	Hydrothermal	$R\bar{3}m$	68
$MA_2AgBiBr_6$ MC	Hydrothermal	$Fm\bar{3}m$	69
MA_2TiBiB_6 MC	Hydrothermal	$Fm\bar{3}m$	70
Sr_2SbTaS_6 MC	Theoretical DFT	$P2_1/n$	71
Sr_2BiNbS_6 MC	Theoretical DFT	$P2_1/n$	71
Sr_2BiTaS_6 MC	Theoretical DFT	$P2_1/n$	71
Ba_2SbTaS_6 MC	Theoretical DFT	$P2_1/n$	71
Ba_2BiNbS_6 MC	Theoretical DFT	$P2_1/n$	71
Ba_2BiTaS_6 MC	Theoretical DFT	$P2_1/n$	71
Ba_2SbTaS_6 MC	Theoretical DFT	$R\bar{3}m$	71
Ba_2BiNbS_6 MC	Theoretical DFT	$R\bar{3}m$	71
$Ba_2BiTaSe_6$ MC	Theoretical DFT	$R\bar{3}m$	71
$Cs_2AgBiBr_6$ single crystal	HBr solution	$Fm\bar{3}m$	71
$Cs_2AgBiBr_6$ MC	Spin coating	$Fm\bar{3}m$	73
$Cs_2AgBiCl_6$ MC	Solid state	$Fm\bar{3}m$	74
$Cs_2AgBiBr_6$ MC	Both solid state and solution based	$Fm\bar{3}m$	75
$Cs_2AgBiCl_6$ MC	Both solid state and solution based	$Fm\bar{3}m$	75
Cs_2AgBiX_6 (X = Cl, Br) MC	Solution process	$Fm\bar{3}m$	76
$Cs_2AgInCl_6$ MC	HCl solution	$Fm\bar{3}m$	77
$Cs_2AgInCl_6$ MC doped with Yb	HCl solution	$Fm\bar{3}m$	77
$Cs_2AgInCl_6$ MC doped with Mn	HCl solution	$Fm\bar{3}m$	78
$Cs_2AgInCl_6$	Hydrothermal	$Fm3m$	79
$Cs_2AgSbCl_6$ MC	HCl solution	$Fm\bar{3}m$	80a
$Cs_2AgSbCl_6$ doped with Cu	HCl solution	$Fm\bar{3}m$	80a
$Cs_2AgInCl_6$ MC	HCl solution	$Fm\bar{3}m$	81
$Cs_2AgBiCl_6$ NC	Anti-solvent reprecipitation	$Fm\bar{3}m$	82
$Cs_2AgBiBr_6$ NC	Anti-solvent reprecipitation	$Fm\bar{3}m$	82
Cs_2AgBiI_6 NC	Anti-solvent reprecipitation	$Fm\bar{3}m$	82
$Cs_2AgInCl_6$ NC	Hot injection	$Fm\bar{3}m$	83
$Cs_2AgSbCl_6$ NC	Hot injection	$Fm\bar{3}m$	83
Mn doped $Cs_2AgInCl_6$ NC	Hot injection	$Fm\bar{3}m$	84
$Cs_2NaIn_xBi_{1-x}Cl_6$:Mn ($0 \leq x \leq 1$)	Hot injection	$Fm\bar{3}m$	85
Cs_2AgBiX_6 NC	Hot injection	$Fm\bar{3}m$	86
Bi doped $Cs_2AgInCl_6$ NC	Hot injection	$Fm3m$	87

optical properties are investigated from several optoelectronic characterizations like band gaps, absorption coefficients, photoluminescence quantum yields, and lifetimes. The energy bandgap of a perovskite material is inversely proportional to the absorption threshold. Therefore, perovskites having higher bandgaps tend to exhibit narrow absorption. Generally, perovskite materials exhibit both direct and indirect bandgaps. The bandgap transition of lead halide perovskites appears mainly due to the ligand to metal charge transfer where the p-orbitals of halides predominate as the valence band maximum (VBM). Charge transfer occurs from the VBM to the conduction band minimum (CBM), which has lead p-orbital character in most of the cases. The electronic configuration of Pb^{2+} ($6s^2 6p^0$) allows the filled 6s orbital to mix effectively with the 5p orbital of the halide ion in the valence band, where the vacant lead 6p orbital acts as the conduction band.[88] DFT calculation revealed that this composition of valence band maxima and conduction band minima contributes to the material's long carrier lifetime and shallow defect states, whereas the high p-orbital based density of states near the band edges is responsible for the strong absorption.[89a,b]

3.1. Optical properties of double perovskite microcrystals

The metal hybrid MA_2KBiCl_6 double perovskite shows two edges in their reflectance spectrum.[68] The Tauc plot determines the apparent optical bandgap value. The UV-visible spectrum exhibits two edges at 3.04 and 3.37 eV for the MA_2KBiCl_6 double perovskite. Yin et al. investigated the optical and electronic properties of chalcogenide double perovskites by calculating the band structures at PBE levels.[71] Through the partial density of states, they established that antibonding coupling occurs between the Sb lone pair 5s and the S 3s at the VBM level similar to $CH_3NH_3PbI_3$. They reported very low bandgaps for the materials. Although an indirect bandgap is not suitable for solar cell application because of the weak optical absorption at the band edge, the reported double perovskites have low bandgaps (ΔE_g), facilitating easy electron–hole transport suitable for cell performance. So far we have discussed the optoelectronic properties of hybrid double perovskites. Now we will consider the optical properties of pure inorganic halide double perovskites.

Karunadasa et al. reported a red orange double perovskite single crystal having a high life time.[72] The material exhibits an indirect bandgap of 1.95 eV (Fig. 7a), which is very much suitable in a tandem solar cell for coupling with a Si absorber. The material has an indirect bandgap in the shallow absorption region beginning at 1.8 eV. This bandgap is slightly lower than the bandgap of $MAPbBr_3$. At room temperature the material shows a weak photoluminescence (PL) peak centred at 1.87 eV, which indicates that it follows a non-radiative recombination pathway (Fig. 7b). Upon decreasing the temperature of the system, the PL intensity increases. At 23 K temperature the
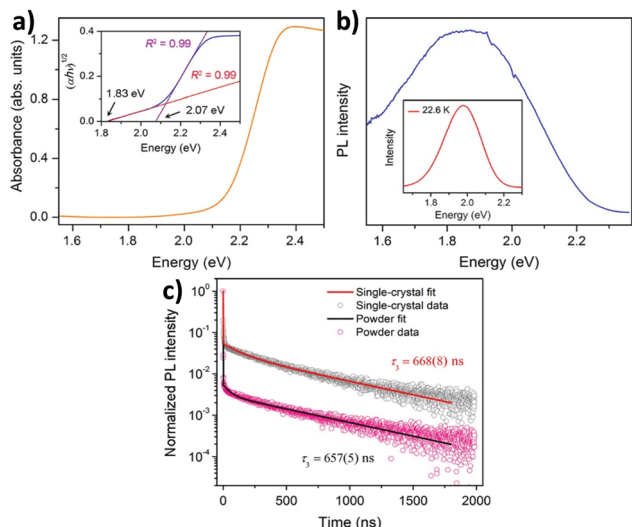
Fig. 7 (a) Absorption spectra, (b) PL spectra and (c) PL decay curves of $Cs_2AgBiBr_6$ double perovskite MCs respectively. Reproduced with permission.[72] Copyright 2016, American Chemical Society.

PL peak is more intense and blue shifted which is observed at 1.98 eV. The material shows a high lifetime of 660 ns (Fig. 7c). This does not vary significantly between the single crystal and powder sample. Therefore, this is the fundamental carrier lifetime of the material.

Guistino *et al.* calculated the bandgaps for a series of double perovskites which lie below 2.7 eV considered as indirect bandgaps.[74] They reported that the band gap value increases randomly on moving up the halogens in the periodic table. This occurs due to the different characters of electronic states at the band edges. The Tauc plot of $Cs_2AgBiCl_6$ shows that the indirect band gap falls in the range of 2.3 to 2.5 eV. The material gives maximum emission at 575 nm or 2.2 eV which is red shifted from the absorption maximum. In addition to that, the time resolved photoluminescence decay curve fitted with the two exponential decay curve having a fast decay time of 15 ns and a slow decay period of 100 ns. The authors reported that the Cl-p and Ag-d characters are predominant in the electronic band structure and conduction band edges split into two bands due to spin–orbit coupling. McClure *et al.* reported $Cs_2AgBiCl_6$ and $Cs_2AgBiBr_6$ which have both direct and indirect bandgaps.[75] The Woodward group reported that the onset of absorption spectra of double perovskites is not sharp as that of lead halide perovskites because of their indirect bandgaps.[75] The band gaps of $Cs_2AgBiCl_6$ and $Cs_2AgBiBr_6$ were 2.77 and 2.17 eV respectively. The authors calculated the band value using the Kubelka–Munk equation, which expresses absorbance as a function of reflectance: $F(R) = \alpha = (1 - R)^2/(2R)$. Here R is the reflectance and α is the optical absorption coefficient. Kar *et al.* established how the fluorescence intensity of double perovskites can be increased only by the addition of water. They reported that the fluorescence intensity of double perovskites gradually increases by the addition of water because the water molecule acts as a surface ligand along with oleic acid. Water, being a polar solvent, can dissolve the

precursor salts more efficiently and increase the PL intensity and consequently the PLQY of the materials increases.[76] Nag *et al.* reported near infra-red emission by doping Yb ions into $Cs_2AgInCl_6$ double perovskite microcrystals.[77] All the microcrystals exhibit an absorption onset at 360 nm (Fig. 8a) of the direct band gap. The authors reported that due to the presence of low percentages of Yb ions in the perovskite hosts there is no shift in the absorption spectra. Yb ion doping results in NIR emission at 994 nm, which increases upon increasing the dopant concentration (Fig. 8b). PLE spectra (Fig. 8c) resemble UV spectra, which indicates that upon light excitation the host double perovskite transfers its excited energy to the dopant f electrons which undergo $^2F_{5/2} \rightarrow {}^2F_{7/2}$ electronic transition to produce NIR emission at 994 nm. PL decay dynamics reveals a single exponential curve (Fig. 8d) with a long material lifetime of 2.7 ms, which is also a characteristic of Yb^{3+} incorporation into the perovskite lattice. Nag *et al.* also reported the increase of fluorescence intensity by doping Mn ions into $Cs_2AgInCl_6$ double perovskite microcrystals.[78] The absorbance value for each sample was 350 nm. An interesting change was observed in the emission wavelength from the undoped to Mn doped double perovskite. Undoped $Cs_2AgInCl_6$ exhibits weak emission at 619 nm, whereas doping with Mn ions produces strong emission centred at 632 nm with an FWHM of 300 meV. The Mn ion doped double perovskites have higher PLQYs up to 5% as compared to undoped samples. The transition of a Mn d electron from the $^4T_1$ to $^6A_1$ state is responsible for the increase of PL intensity after doping with Mn ions in the double perovskite. Mn doping also causes a significant increase of lifetime in the materials up to 974 μs. This high lifetime is accounted for by the spin forbidden transition of $^4T_1$ to $^6A_1$ of Mn d electrons in the Mn^{2+} doped $Cs_2AgInCl_6$ double perovskite.[78] Liu *et al.* calculated the bandgap of $Cs_2AgInCl_6$ using the Kubelka–Munk function.[79] The material consists of

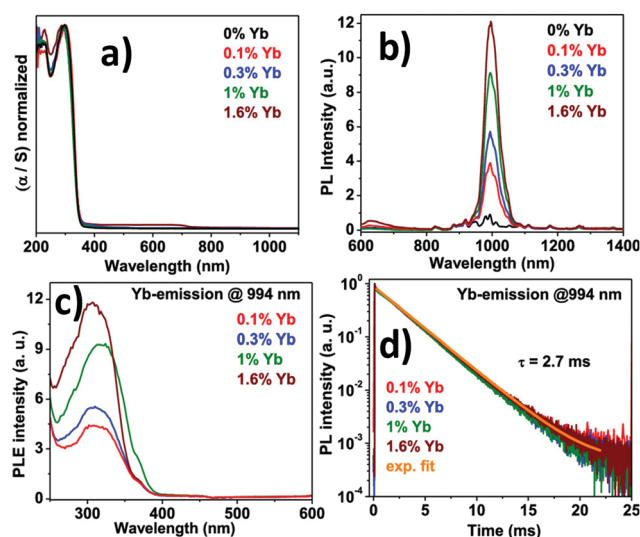**Fig. 8** (a) Absorption spectra, (b) PL spectra, (c) PLE spectra, and (d) PL decay dynamics of Yb doped $Cs_2AgInCl_6$ double perovskite MCs. Reproduced with permission.[77] Copyright 2019, American Chemical Society.

two distinct bands at 335 and 370 nm with a direct bandgap of 3.23 eV. Under 370 nm irradiation, the double perovskite exhibits broad red emission at 635 nm wavelength, which appears due to photo-induced defects in $Cs_2AgInCl_6$. The bi-exponential decay curve of the material has a slower decay lifetime of 16.3 µs and a longer decay period of 100 µs. With the help of excitation power dependent PL analysis, Liu *et al.* noticed that a well-defined PL peak is observed at 596 nm at 0.28 ms, which shifts towards a higher wavelength by increasing the delay time. This fact is attributed to the presence of filled subgap states at this timescale.

Michaleis *et al.* reported how the indirect bandgap of double perovskites can be reduced by doping with heterovalent metal ions.[80a] Doping Cu^{2+} ions into $Cs_2AgSbCl_6$ results in a dramatic shift in the optical bandgap of the double perovskite. The parent molecule shows an indirect bandgap of 2.65 eV in the diffuse reflectance spectrum, which decreases to 1.02 eV upon doping with Cu^{2+} ions in the double perovskite host. A drastic visual colour change is observed from yellow to black by doping with Cu ions. The reduction of the bandgap is further attributed to the absorption in the near IR region. Also, the band edge of the doped material is not sharp like the parent material due to the lattice disorders. Guistino *et al.* reported a direct bandgap $Cs_2AgInCl_6$ double perovskite semiconductor which turns from white to orange under UV light illumination due to photoinduced electronic or structural changes.[81] This happens because of the strong sensitivity of the electronic structure of $Cs_2AgInCl_6$. The authors reported the square modulus of the electronic wave function at the band edges, which shows that the bottom of the conduction band is associated with the Cl-3p and In-5s/Ag-5s states, whereas the top of the valence band is comprised of the Cl-3p and In-4d/Ag-4d states. The material shows the first absorption maximum at 380 nm or 3.3 eV and the second absorption band at 585 nm or 2.1 eV. It exhibits a well-defined PL peak centred at 608 nm or 2.04 eV with an FWHM of 120 nm or 0.37 eV. The reported double perovskite exhibits a fast relaxation lifetime of 1ns and a slow decay time for a period of 6 µs. According to the literature, generally most of the Cs_2AgBiX_6 double perovskites fall in the indirect bandgap region, while $Cs_2AgInCl_6$ lies in the direct bandgap region. However, Bein *et al.* reported a direct bandgap $Cs_2AgBiBr_6$ double perovskite thin film. Absorption spectra of the material exhibit a peak around 550 nm wavelength, which corresponds to an E_g of 2.21 eV.[89c] A time-correlated single photon counting (TCSPC) study shows that the $Cs_2AgBiBr_6$ powder has a lifetime of 568 nm, whereas the film has a decay period of over 220 ns. The PL intensity of the $Cs_2AgBiBr_6$ powder is quenched approximately 60% on TiO_2, while the reduction of intensity is observed more than 80% in the presence of spiro-OMeTAD. Until now, we have observed that several studies reveal a large number of E_g values, which mainly originate from different synthetic procedures along with the variable methods of measurement.

### 3.2. Optical properties of double perovskite nanocrystals

The optical properties of double perovskite nanocrystals are little bit different from the optical properties of double perovskite microcrystals. Let us discuss the similarities and differences between these two analogues of double perovskites.

The bandgap reduction in double perovskite nanocrystals was reported by Zang *et al.* in 2020.[80b] Here Cu doping into $Cs_2AgInCl_6$ leads to the lowering of the bandgap in the double perovskite from 3.60 eV to 2.19 eV. Generally, the VBM of $Cs_2AgInCl_6$ is formed from the hybridization of Ag-4d and Cl-3p orbitals, whereas the CBM arises from the antibonding In-s orbital. Upon doping Cu^{2+} ions into the double perovskite, the Cu-3d orbital participates in the formation of the VBM and remains in the higher state than the Ag-4d orbital although the position of the CBM remains unchanged. Consequently, the bandgap value decreases. As a result of this, decreases in PL intensity and lifetime are observed. Han *et al.* reported Cs_2AgBiX_6 double perovskite nanocrystals which exhibit tunable emission in the range of 395 to 575 nm.[82] They demonstrated a new phenomenon to increase the emission intensity of the perovskite nanocrystals by increasing the amount of oleic acid (OA) as a ligand during the formation of nanocrystals. Ligand free $Cs_2AgBiBr_6$ nanocrystals show an exciton peak at 440 nm wavelength (Fig. 9a). There is a long absorption tail up to 700 nm which appears due to the presence of sub-bandgap transitions caused by the existence of surface defects. These surface defects can be suppressed by the addition of surfactants such as oleic acid. Ligand free $Cs_2AgBiBr_6$ exhibits double emission peaks at 465 nm and 510 nm wavelengths (Fig. 9c). Upon increasing the content of oleic acid, the peak at 510 nm decreases, whereas the peak at 465 nm increases, which suggests that the emission peak that appears at 465 is due to band edge emission. Sub-band gap trap states are responsible for the 510 peak. The relative PL intensity (ratio of the PL intensity at the peak position of 510 nm to that of 465 nm) decreases like relative absorption (Fig. 9b). The PL intensity for all the halide nanocrystals was increased by the addition of an excess amount of oleic acid. The PLQY also increases with the increase of PL intensity due to the suppression of the non-radiative transition. The authors reported that $Cs_2AgBiBr_6$ exhibits maximum emission when 12% oleic acid is added, with the maximum PLQY of 0.7%, while $Cs_2AgBiCl_6$ exhibits the highest emission in the presence of 8% oleic acid. TCSPC measurement informs that the nanocrystals show tri-exponential decay where the long lived component is responsible in higher percentages at long PL wavelengths (Fig. 9d). When nanocrystals are synthesized in the presence of xylene and metal acetate, they exhibit interesting optical features.[83] $Cs_2AgInCl_6$ nanocrystals have an absorption shoulder in the range of 290 to 310 nm wavelengths and band gaps of 4.15 ± 0.05 eV for diluted samples. Nanocrystals have broad emission at 567 nm due to the Laporte forbidden 4d → 5s transition at the band edges and a PLQY of 0.6%. On the other hand, $Cs_2AgSbCl_6$ nanocrystals show absorption at wavelengths of 360 and 300 nm. The Tauc plot shows that the nanocrystals have a band gap of 2.83 ± 0.02 eV. $Cs_2AgSbCl_6$ nanocrystals have weak emission at 300 nm due to the momentum forbidden transition because of the indirect band gap. Optical studies indicate that the nanocrystals have confinement energies of 0.7 eV for $Cs_2AgInCl_6$ and 0.3 eV for $Cs_2AgSbCl_6$ in
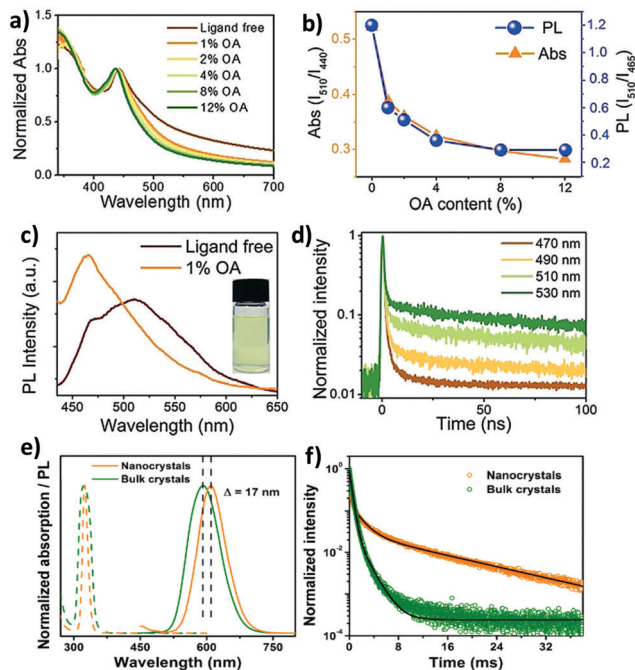
Fig. 9 (a) Absorption spectra of ligand-free and OA capped $Cs_2AgBiBr_6$ NCs, (b) the variation of relative PL and relative absorption (ratio of the absorption at 510 nm to that at 440 nm), (c) PL spectra of ligand-free and 1% OA capped NCs (photograph of the colloidal ligand-free $Cs_2AgBiBr_6$ NCs), and (d) TR-PL kinetics of ligand-free $Cs_2AgBiBr_6$ NCs. Reproduced with permission.[82] Copyright 2018, Wiley-VCH. (e) Steady-state absorption (dashed lines) and PL (continuous lines) spectra of $Cs_2NaIn_{0.75}Bi_{0.25}Cl_6$:Mn NCs (orange) and bulk crystals (olive green), and (f) TR-PL decay curves of $Cs_2NaIn_{0.75}Bi0.25Cl_6$:Mn NCs ($\tau_{avg}$ = 8.7 ms) and bulk crystals (τ_{avg} = 0.6 ms). Reproduced with permission.[85] Copyright 2020, American Chemical Society.

the absorption spectra with Bohr exciton radii of 1.02 nm and 0.82 nm, respectively, for diluted nanocrystals. However, concentrated nanocrystals exhibit an indirect gap of 2.57 ± 0.05 eV for $Cs_2AgSbCl_6$ and a direct gap of 3.57 ± 0.03 eV for $Cs_2AgInCl_6$ like bulk samples. In general, double perovskites have low photoluminescence quantum yields, which can be increased by doping with heterovalent metal ions. We are going to discuss the various strategies briefly. For this purpose, Manna *et al.* reported doping of Mn ions into $Cs_2AgInCl_6$ double perovskite nanocrystals.[84] The authors observed an absorption onset at 350 nm for both the undoped and doped nanocrystals corresponding to band gaps of 4.36–4.38 eV. Although the absorption spectra are similar in nature, the corresponding PL spectra differ from each other. Undoped nanocrystals have broad weak PL emission at 560 nm with a PLQY of $1.6 \pm 1\%$, while Mn doped nanocrystals show strong bright orange emission at 620 nm with a PLQY value of $16 \pm 4\%$. Mn doping produces $^4T_1 \rightarrow {}^6A_1$ transition in the double perovskite host, which results in a shift of the broad emission from 560 nm to 620 nm. Time resolved (TR) PL analysis revealed microsecond long photoluminescence which is a characteristic of the spin forbidden nature of Mn^{2+} luminescence that occurs due to intersite energy-transfer between Mn centres. Homovalent metal ion (Yb^{3+} ion) doping into $Cs_2AgInCl_6$ can produce NIR

emission which is very significant for optoelectronic applications.[77] UV-visible spectra of undoped and Yb doped $Cs_2AgInCl_6$ have similar features and exciton absorption occurs at 345 nm. PL spectra of the samples reveal that the Yb doped double perovskite can produce emission in the NIR region, while the undoped sample shows weak emission only in the visible region at 607 nm. The f electrons of the dopant Yb ion cause NIR emission. Here transition occurs from $^2F_{5/2}$ to $^2F_{7/2}$ and PLQY increases. The PL decay curve informs that Yb doped nanocrystals show bi-exponential decay with a long life time of 3 ms and a comparatively short life time of 749 μs. Han *et al.* established how Mn doping can tune the PL spectra of inorganic halide double perovskite nanocrystals from yellow to bright orange red photoluminescence with a maximum quantum efficiency (PLQE) of 44.6%.[85] Undoped $Cs_2NaIn_xBi_{1-x}Cl_6$ $(0 < x < 1)$ nanocrystals show absorption and PL emission peaks at 324 nm and 424 nm wavelengths respectively. Undoped nanocrystals have a low PLQY, which increases upon doping with Mn ions. The PL peak of Mn doped nanocrystals shifts from 583 to 614 nm (Fig. 9e) due to the spin forbidden transition of Mn^{2+} ions involving $^4T_1 \rightarrow {}^6A_1$ transition. Doping of Mn ions into the double perovskite nanocrystals results in an increase of emission wavelength as compared to the bulk, which is contradictory to the quantum confinement effect. The authors reported that the d–d transition of Mn^{2+} is responsible for this opposite observation. However, the PL lifetime also increases in the nanocrystals than the bulk materials (Fig. 9f). Gamelin *et al.* reported indirect bandgap perovskite nanocrystals.[86] The absorption peaks for $Cs_2AgBiCl_6$ and $Cs_2AgBiBr_6$ nanocrystals occur at 3.39 and 2.87 eV respectively. Both the samples have weak broad orange photoluminescence with PLQYs of $0.3 \pm 0.3\%$. Sometimes it is observed that the PL intensity of the double perovskite increases upon decreasing the temperature due to the decrease of trap states in the molecules.

The Gamelin group reported the same observation. They noticed that emission of the nanocrystals brightens at cryogenic temperature. At 20 K $Cs_2AgBiCl_6$ nanocrystals show a single broad emission band centred at 1.68 eV, while the $Cs_2AgBiBr_6$ spectrum has two emission bands, a broad band centred around 1.75 eV, and a more intense, narrower feature centred at 1.97 eV. It is confirmed through photoluminescence exciton spectra that the same species is responsible for the absorption and emission spectra for both the nanocrystals. The broad band in the nanocrystals appears mainly from defect or surface related states. As compared to bulk species, nanocrystals have more surface trapping states which are suppressed upon decreasing the temperature of the system and consequently increase the decay time of the luminescence. Therefore, $Cs_2AgBiBr_6$ nanocrystals show a decay time of <100 ns at 150 K temperature, which increases up to 1.4 μs at 82 K. On the other hand, homovalent doping on $Cs_2AgInCl_6$ can tune the emission spectra. The Aswani Yella group reported how Bi doping can tune the emission spectra from white to orange.[87] The band gap decreases upon increasing the Bi dopant concentration and its nature changes from direct to indirect. $Cs_2AgInCl_6$

nanocrystals involve the formation of valence band maxima by the contribution of Ag 4d and Cl 3p orbitals, while the conduction band is constructed from the hybridization of Ag 5s, In 5s, and Cl 3p orbitals. In the case of the Bi based double perovskites, the VBM is formed by the hybridization of Ag 4d and Cl 3p orbitals and a conduction band maximum is formed with Bi 6p orbitals. The difference in character of the conduction band is responsible for the change in band gap nature on changing the ion involved in the formation of double perovskites. Therefore, $Cs_2AgInCl_6$ nanocrystals have a direct band gap of 3.46 eV and the Bi doped perovskite has a bandgap of 2.9 eV. This band transition occurs for the 30% or above 30% Bi doped double perovskite. However, except for the undoped nanocrystal, all Bi doped nanocrystals show an absorption maximum at 360 nm, which appears due to band edge absorption. The intensity of absorption increases upon increasing the dopant concentration. The authors excited all the compounds at 380 nm wavelength to record the fluorescence spectra. Nonemissive pure nanocrystals show white emission by doping with Bi ions. At low concentrations of Bi ions, the peak occurs in the range of 570 to 620 nm due to self-trap transition, which is attributed to the Jahn–Teller distortion of the [AgCl₆] octahedron in the excited state. At high concentrations of Bi ions, the emission peak appears only at 420 nm due to band edge emission. In the case of the 15% and 30% Bi doped nanocrystals, both the band edge and sub-band gap defect level emissions occur. Nanocrystals have the highest lifetime of up to 17 ns for 60% Bi doped samples. However, it is clear from the above discussion that with the minimal change in the conduction band, the conduction band character can be tuned between s and p orbitals. In 2017, Tran *et al.* showed how to achieve a convergence of direct to indirect band gaps by the adjustment of conduction band maxima between s and p orbitals.[90] Fig. 10 clearly shows that the bandgap decreases when we go from direct to indirect bandgaps. Here the bandgap value decreases from In to Sb halides. Likewise, the E_g value decreases from indium to bismuth based perovskites.

4. Morphological studies

The morphologies of double perovskites have attracted the attention of researchers due to their interesting orientation, shape and size. The size and shape of double perovskites are highly dependent on the reaction process, *i.e.* the nature of the solvent used, the temperature of the system, and the heating or cooling rate. We will discuss thoroughly the morphologies of double perovskite microcrystals and nanocrystals in this section.

4.1. Morphology of double perovskite microcrystals

Lei *et al.* reported a $Cs_2AgBiBr_6$ thin film.[73] The film has a high coverage rough surface with an average grain size of 100 nm. There are undesired pinholes in the surface due to the restricted diffusivity of the precursor materials in the solvent drying stage at the time of spin-coating.
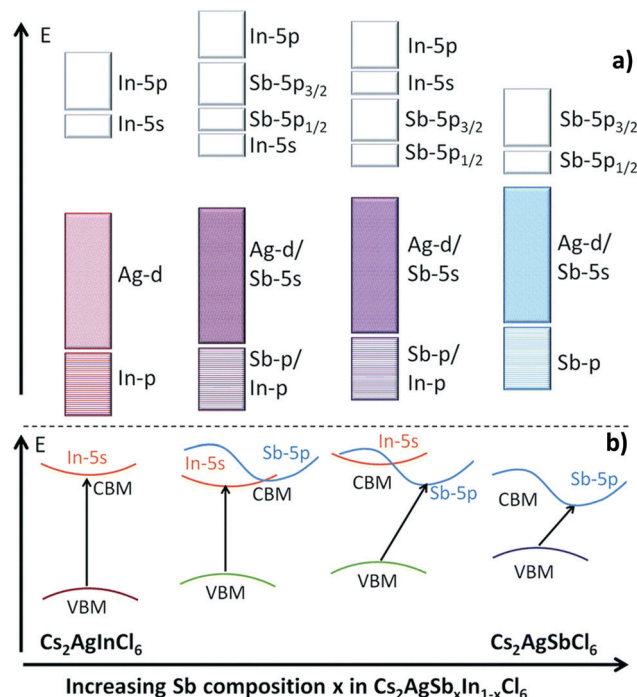

Fig. 10   (a) Schematic diagram of the bonding and antibonding orbitals of $Cs_2AgSb_xIn_{1-x}Cl_6$ and (b) transition from direct to indirect bandgaps on changing the character of the VBM and CBM. Reproduced with permission.[90] Copyright 2017, Royal Society of Chemistry.

Different morphologies of double perovskite microcrystals have been reported in the literature. However, tuning of the morphology of double perovskites is rare. Recently, Kar *et al.* invented an interesting way to tune the morphology of Cs_2AgBiX_6 (X = Cl, Br) double perovskite microcrystals.[76] They observed that microcrystals are quasispherical in nature in organic medium. The morphology is tuned from quasi-spherical to quasi-octahedral on changing the reaction medium. This happens due to the presence of water molecules on the surfaces of the microcrystals which act as surface ligands along with oleic acid. Water molecules dissociate into hydroxyl ions and H_3O^+. Hydroxyl ions can replace oleate ions from the surfaces of the perovskite, which affects the growth of microcrystals and results in changes in shape and size of the microcrystals. $Cs_2AgBiCl_6$ changes its shape from quasi-spherical (Fig. 11a and b-HRTEM) to quasi-octahedron (Fig. 11c and d-HRTEM), while $Cs_2AgBiBr_6$ aggregates (Fig. 11e and f) itself. Nag *et al.* reported undoped and Yb doped $Cs_2AgInCl_6$ microcrystals in 2019.[77] Growth of all the microcrystals occurs in multifaceted directions. The authors noticed that there is no change in shape and size of the double perovskite upon increasing the dopant concentration. Liu *et al.* reported $Cs_2AgInCl_6$ double perovskite microcrystals obtained by a solvothermal reaction process continued for 12 h.[79] Microcrystals have a regular orthorhombic dodecahedral shape with an average size of 5 μm to 12 μm (Fig. 12a). The material has an fcc crystal with a tetrahedral crystallization habit which can form a truncated octahedral shape. The authors also determined the (111) and (100) planes from the
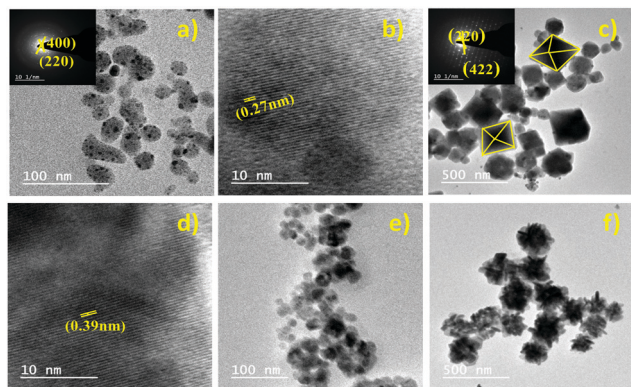
Fig. 11 $Cs_2AgBiCl_6$ MCs: (a) TEM image (SAED pattern inset) and (b) HRTEM image in organic medium and (c) TEM image (SAED pattern inset) and (d) HRTEM image in aqueous medium. $Cs_2AgBiBr_6$ MCs: TEM images in (e) organic medium and (f) aqueous medium. Reproduced with permission.[76] Copyright 2021, Elsevier.

facets of $Cs_2AgInCl_6$ microcrystals (Fig. 12b). They also reported 1.5 mm sized single crystals having a regular octahedral shape obtained by the hydrothermal reaction process continued for 72 hours (Fig. 12c and d). This observation suggests that the size of the single crystal can be changed by changing the reaction conditions. Pristine and Cu doped $Cs_2SbAgCl_6$ have been successfully reported in the literature.[80a] Here the morphology remained unchanged upon doping with heterovalent metal ions although the colour of the microcrystal changed (Fig. 12e). Micrometre sized polycrystals show microfaceted crystal growth (Fig. 12f).

4.2. Morphology of double perovskite nanocrystals

The morphology of nanocrystals is somewhat different from that of microcrystals. The morphology of microcrystals is generally analysed by scanning electron microscopy (SEM), whereas transmission electron microscopy (TEM) is used to investigate the shape and size of double perovskite nanocrystals.

$Cs_2AgBiBr_6$ nanocrystals which were synthesized in 2018 by a solution based procedure had a quasispherical shape with an average size diameter of 5.0 nm and a size distribution of 1.0 nm. These nanocrystals were highly crystalline in nature.[82]

Manna *et al.* reported undoped and Mn doped $Cs_2AgInCl_6$ double perovskite nanocrystals (Fig. 13).[84] Pristine nanocrystals consisted of 9.8 nm cubic shaped particles. Although there is no change in the shape of nanocrystals upon doping with Mn ions, their size increases to some extent. Mn doped nanocrystals are 11–12 nm in size with uniform distribution of Mn ions throughout the lattice of the double perovskite.

According to the literature it has been observed that most of the double perovskite nanocrystals are formed with a cubic shape. Similarly, undoped and Mn doped $Cs_2NaIn_xBi_{1-x}Cl_6$ nanocrystals have a cubic shape with an edge length of 10.59 nm and a mean size of 10.93 ± 0.9 nm.[85] The Gamelin group reported how the size of nanocrystals can be tuned by the variation of solvent from which nanocrystals are precipitated or
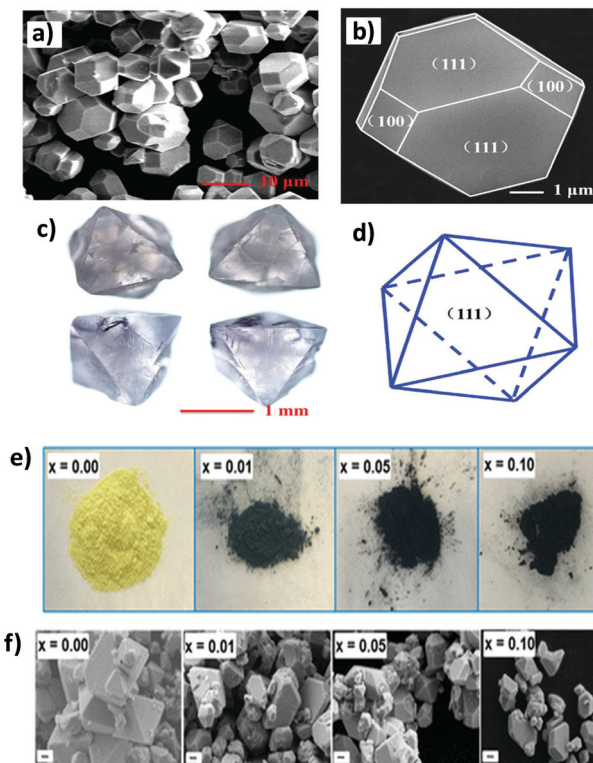
Fig. 12 $Cs_2AgInCl_6$ MCs: (a) and (b) SEM images for 12 h reaction at different magnifications, (c) $Cs_2AgInCl_6$ single crystal for 72 h reaction and (d) simulated crystal faces for one crystal particle.[79] Copyright 2017, Royal Society of Chemistry. Undoped and Cu^{2+} doped $Cs_2SbAgCl_6$ MCs: (e) photographs and (f) FESEM images of polycrystalline materials, where *x* is the nominal Cu^{2+} loading. Reproduced with permission.[80a] Copyright 2018, American Chemical Society.

extracted.[86] They synthesized the nanocrystals by a hot injection method. After successful synthesis and centrifugation, when the particles were extracted from toluene, it was observed that the resulting particles were in cubic shape with an edge length of 8 nm and had narrow size distribution. On the other hand, when nanoparticles were extracted and precipitated from hexane, the obtained particles had relatively broad size distribution with an average edge length of 13 nm. Therefore, the particle size, shape and distribution of double perovskites can be successfully tuned by the change of solvent during the synthesis of materials.

Yella *et al.* reported Bi doped $Cs_2AgInCl_6$ double perovskite nanocrystals. Pure $Cs_2AgInCl_6$ has a cubic shape which changes upon increasing the concentration of Bi dopant (Fig. 14a–o).[87] For different contents of Bi ions, nanocrystals have different shapes such as cubic particles, a mixture of cubic and pentagonal particles, and hexagonal-shaped particles. When 30% Bi was doped, the nanocrystals again remained in cubic shape. The SAED pattern of the materials show the highly crystalline nature of the nanocrystals. The authors also compared the TEM and XRD analysis and they found that all the double perovskite nanocrystals were formed from the pure cubic phase with no traces of impurities. So far we have discussed how the size of the double perovskite can be changed by changing the solvent.
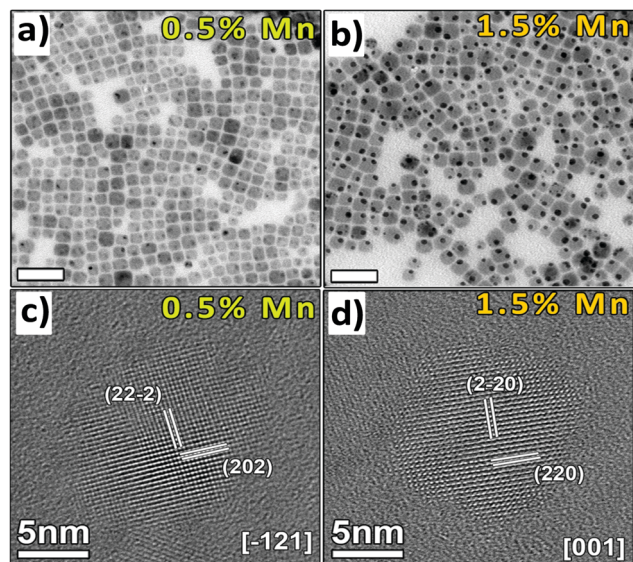
Fig. 13 TEM images of (a) 0.5% and (b) 1.5% and HRTEM images of (c) 0.5% and (d) 1.5% Mn-doped Cs$_2$AgInCl$_6$ NCs respectively. Reproduced with permission.[84] Copyright 2018, American Chemical Society.

Now we will focus on the influence of temperature during the synthesis and its effect on the size of the double perovskite. Wu et al. demonstrated the role and consequence of postannealing in/on the surface morphology and crystallinity of Cs$_2$AgBiBr$_6$ perovskite thin films.[91] SEM and AFM images show that the grain size and crystallinity of the perovskite increase gradually with the increase of the temperature of the post-annealing process (Fig. 14p–y). Due to solid state dewetting (preferential diffusion of the component away from grain boundaries), the roughness of the film increases upon increasing the post-annealing temperature. Without annealing, the as-prepared film has a grain size of 50 nm with an average size of 38 nm, which increases after post-annealing. The average size is 50 nm at 150 °C, which changes to 410 nm at 300 °C. Therefore, the grain diameter changes from the nanosize to microsize by the annealing process due to the structural reconstruction of the double perovskite.

5. Stability

Hybrid lead halide perovskites are unstable under atmospheric conditions. They are prone to degrade in the presence of heat, water, and sunlight and easily convert back to their corresponding precursor materials. Inorganic halide perovskites (CsPbBr$_3$) are more stable than methyl ammonium halide perovskites. However, they suffer from the toxicity issue due to the presence of toxic lead cations. In addition to all the facts, double perovskites are more stable because of their moisture and heat resistance capability. However, when we think about the stability of halide double perovskites, a lot of factors such as thermodynamic stability, mechanical stability, chemical stability, and device stability need to be considered. Halides play an important role in the thermo-dynamics of double perovskites. Down the group, i.e. from Cl to I,

the thermodynamic stability decreases.[92,93] In this section we will discuss the stability of double perovskite materials in different media and under various conditions.

5.1. Stability of double perovskite microcrystals

Inorganic halide double perovskites show good stability because of their inorganic counterions. Slavney et al. compared the stability of Cs$_2$AgBiBr$_6$ crystals with MAPbBr$_3$.[72] They exposed the synthesized material to light and moisture and noticed changes in P-XRD under different conditions. It was reported that there was small surface decolourization for some of the irradiated samples after 15 days due to the sensitivity of silver to the light which recovered its original colour upon storing the samples in ambient light for 2 days. No decomposition of the overall material was observed after exposing it to sunlight and humidity. Similarly, degradation in light due to the presence of silver ions has been reported in many articles for Cs$_2$AgBiCl$_6$,[75] Cs$_2$AgSbCl$_6$,[94] etc. The crystals of Cs$_2$AgBiBr$_6$ were stable up to 430 °C and no phase transition within this temperature was observed. This kind of highly thermally stable material is very useful for solar cell applications.[72] Several groups have reported the chemical and thermal stability of Cs$_2$AgBiCl$_6$ and Cs$_2$AgBiBr$_6$. However, Cs$_2$AgBiI$_6$ is unstable[60,95] like MAPbI$_3$ due to the negative impact of I$^-$ ions[96] in the decomposition process. Therefore, it is very hard to synthesise iodide based double perovskites unlike their chloride and bromide analogues. Liu et al. reported the chemical as well as light and thermal stability of Cs$_2$AgInCl$_6$ double perovskite microcrystals by exposing them to light and moisture, and the stability was confirmed by performing P-XRD in 7, 14 and 26 day intervals (Fig. 15a).[79] The authors found no change in thermal and chemical stability with respect to the crystal size although there is evolution of the AgCl impurities in XRD spectra upon increasing the exposure time. Along with the crystal stability, the thermal stability of the perovskite is very important for optoelectronic applications. According to the literature, the material is relatively stable up to 400 °C (Fig. 15b). A small hump at 200 °C occurs because of some water molecules absorbed in the surface of the perovskite. A major change occurs from 400 to 615 °C with a weight loss of 42.64 wt%. In the DSC curve, an exothermic peak occurs at 539 °C due to the evaporation of CsAgCl$_2$. The decomposition process of Cs$_2$AgInCl$_6$ can be thought of in the following way:

$$Cs_2AgInCl_6 \rightarrow CsAgCl_2 + CsInCl_4$$

CsInCl$_4$ can further be dissociated into CsCl and InCl$_3$. AgCl and CsCl evaporate around 752 °C. This is the third weight loss in the DSC curve which is observed in between 650 and 1000 °C. Our group recently disclosed that double perovskite microcrystals prepared in organic medium were stable up to two months (Fig. 15c and d).[76] It was also noticed that the materials were simultaneously stable beyond months when the materials were synthesized in a mixture of aqueous and organic media (Fig. 15e). We stored the synthesized microcrystals in the laboratory under ambient conditions and checked their crystal stability by
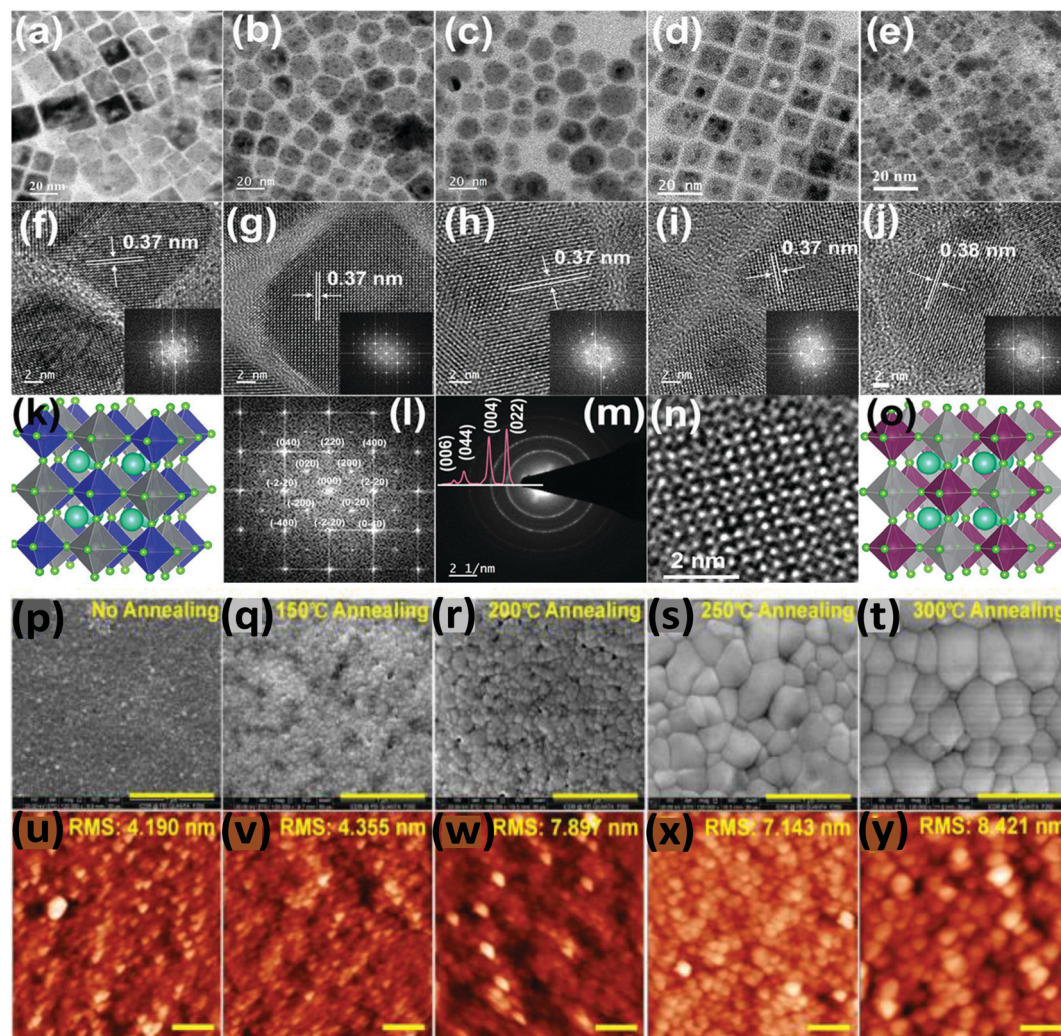
Fig. 14 TEM images of $Cs_2AgIn_{1-x}Bi_xCl_6$ at different doping concentrations of Bi: (a) 0% Bi, (b) 5% Bi, (c) 15% Bi, (d) 30% Bi, and (e) 100% Bi; the corresponding HRTEM images and FFT spectra (f–j); simulated FFT and SAED patterns of 5% Bi (l and m); crystal structures of $Cs_2AgInCl_6$ and $Cs_2AgBiCl_6$ (k and o); and atomic resolution of the 30% Bi-doped nanocrystals (n). Reproduced with permission.[87] Copyright 2019, American Chemical Society. $Cs_2AgBiBr_6$ films annealed at different temperatures: (p–t) SEM and (u–y) AFM. Reproduced with permission.[91] Copyright 2018, Wiley-VCH.

performing P-XRD every week. No decomposition peaks for any starting material or impurities were found in the XRD spectra.

This observation indicates that, unlike lead halide perovskites, double perovskites are simultaneously stable in organic medium as well as a mixture of aqueous and organic media, which is helpful for optoelectronic applications. Michaelis *et al.* observed the long-term stability of the $Cs_2AgSbCl_6$ double perovskite in an outstanding way.[80a] They examined both the moisture and thermal stability of the double perovskite in different atmospheres for the parent and Cu^{2+} doped $Cs_2AgSbCl_6$ double perovskite microcrystals. The polycrystalline undoped and 10% Cu doped materials were stable up to 365 and 30 days, respectively, under 55% relative humidity. There was no decomposition peak in the absorption, NMR and P-XRD spectra (Fig. 16a and b). The thermal stability determined by a TGA experiment revealed that the polycrystalline undoped material was stable up to 250 °C (Fig. 16c).

The compound is stable even after heating at 110 °C for 6 days. So it can be stated that these compounds show high optical and structural stability in every aspect. $Cs_2AgBiBr_6$ double perovskite can maintain its crystal phase purity for several months. However, the material degrades easily by alloying with another metal ion such as Tl due to the mixing of ionic and covalent bonding.[97] Halide double perovskite based devices are stable up to several months or weeks. Ning *et al.* demonstrated that $Cs_2AgBiBr_6$ based solar cells are stable over 25 days under both dark and ambient conditions.[98] A $Cs_2AgBiBr_6$ perovskite solar cell was reported to be stable for four months under ambient conditions.[99] Double perovskite based devices have the capacity to retain their stability under continuous illumination under ambient conditions.[98,99] Double perovskites used for X-ray detectors also show good stability under ambient conditions without any encapsulation.[100]

5.2. Stability of double perovskite nanocrystals

The variation of solvent can affect the stability of double perovskite nanocrystals by different ways. Perovskite
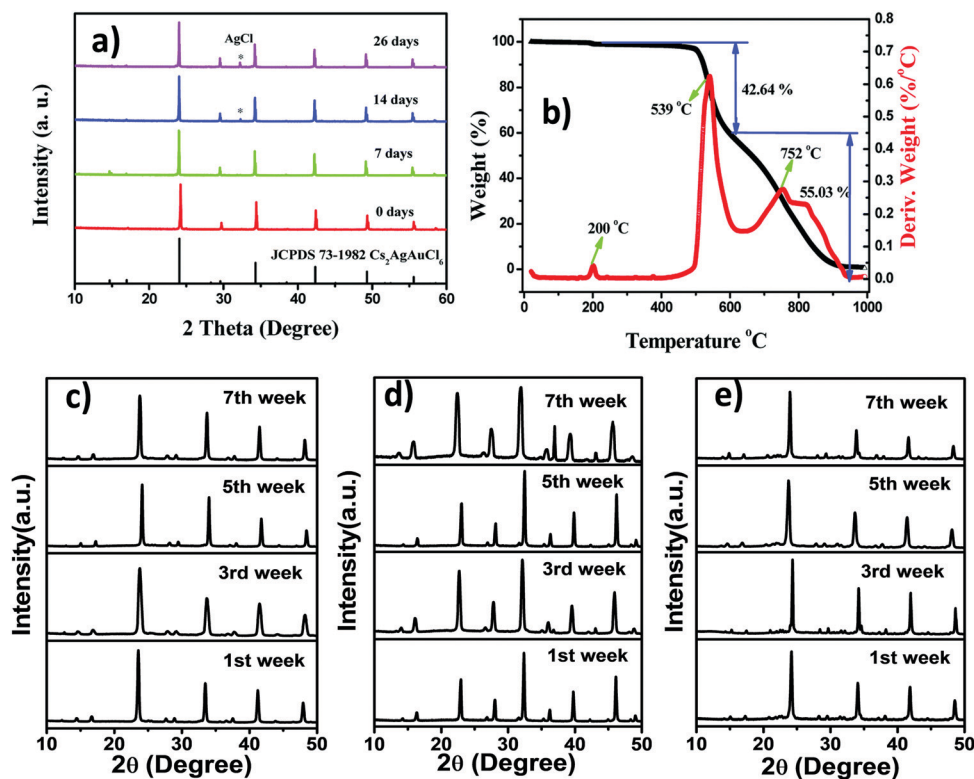
Fig. 15 $Cs_2AgInCl_6$ MCs: (a) P-XRD patterns at 7, 14 and 26 day intervals, and (b) TGA and DSC curves. Reproduced with permission.[79] Copyright 2017, Royal Society of Chemistry. P-XRD patterns of (c) $Cs_2AgBiCl_6$ MCs and (d) $Cs_2AgBiBr_6$ MCs in organic medium, and (e) $Cs_2AgBiBr_6$ MCs in a mixture of aqueous and organic media. Reproduced with permission.[76] Copyright 2021, Elsevier.

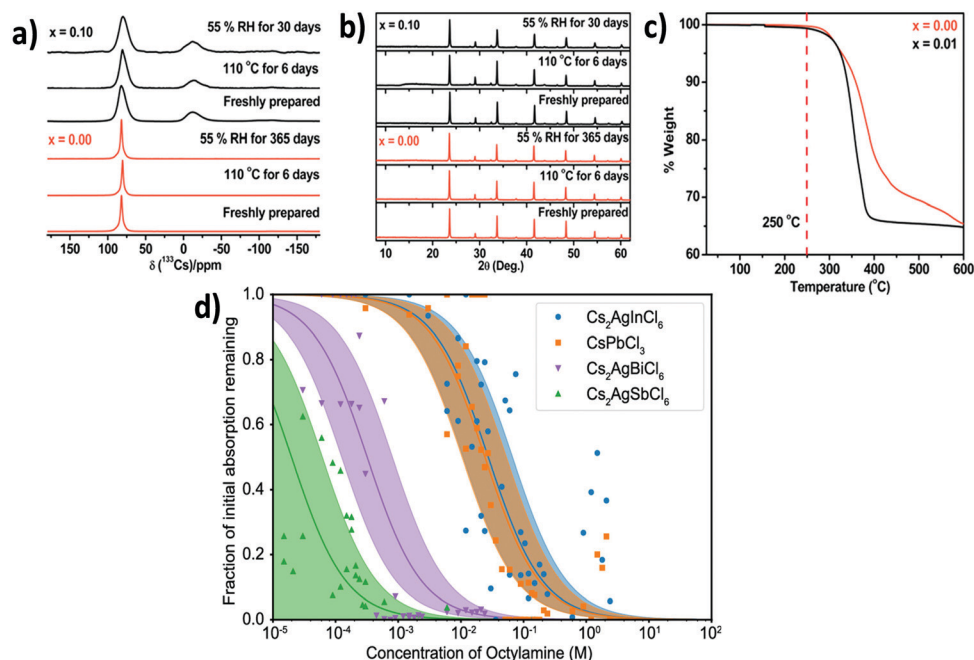**Fig. 16** (a) NMR, (b) P-XRD and (c) TGA spectra of undoped and Cu doped $Cs_2AgSbCl_6$ MCs. Reproduced with permission.[80a] Copyright 2018, American Chemical Society. (d) Stability analysis of $Cs_2AgSbCl_6$, $Cs_2AgInCl_6$, $Cs_2AgBiCl_6$ and $CsPbCl_3$ NCs by amine titration. Reproduced with permission.[83] Copyright 2019, American Chemical Society.

nanocrystals can decompose rapidly in highly polar solvents like *N,N*-dimethyl formamide and acetone due to their tendency to dissolve ion type perovskites.[101]

Protonic isobutanol can ease the proton exchange between oleic acid and oleylamine used for the synthesis of nanocrystals and results in a dynamic equilibrium between surface bound and free ligands.[102] By this way, isobutanol can impart more stability to the nanocrystals as compared to acetone. Due to the low polarities and dielectric constants of chloroform and octane, the nanocrystals are stable in these solvents for several weeks. Zhou *et al.* proclaimed the stability of $Cs_2AgBiBr_6$ nanocrystals under moisture, high temperature, 55% relative humidity and dark conditions.[103] There was no peak of the decomposition material in the XRD spectrum after storing the perovskite for 90 days. The compound is also sustainable at 100 °C in a dry N_2 atmosphere for 300 hours and constant illumination (700 mW cm^{-2}) for 500 hours. These results validate that the nanocrystals are very much tolerant to the heat, moisture and light, which is very meaningful for a wide range of optoelectronic applications. Aliviasto *et al.* demonstrate the quantitative stability of perovskite nanocrystals by a comparison method through titration assay where $Cs_2AgSbCl_6$, $Cs_2AgInCl_6$, $Cs_2AgBiCl_6$ and $CsPbCl_3$ NCs were titrated with amines based on the decomposition reaction of halide perovskites with the amines (Fig. 16d).[83] Double perovskites undergo reaction with amines in the following way:

$$Cs_2AgMCl_6 + RNH_2 \leftrightarrow MCl_3RNH_2 + Cs_2AgCl_3$$
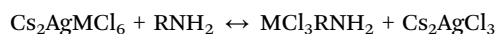
In addition to the structural measurement, the stability of perovskites can also be checked by the optical and morphological studies. Sometimes alloying results in lower stability of double perovskites. Chen *et al.* reported that Mn and Yb doping on double perovskite nanocrystals could change the photoluminescence of the materials,[104] whereas their stability remained unchanged. All the samples were stable up to three weeks and this was confirmed by structural, optical and morphological studies (Fig. 17).

6. Application of double perovskites

Lead-free double perovskites have not been explored vastly in respect of their application as compared to lead halide perovskites because a lot of research is ongoing to understand the structural and fundamental photo-physical properties of these materials properly. In spite of these obstacles, they have attracted excellent research attention in various optoelectronic applications.

$Cs_2AgBiBr_6$ single crystals can be successfully applied for solar cells due to their indirect bandgap of 1.95 eV, which is suitable for coupling with a Si absorber in a tandem solar cell.[72] Single crystals of $Cs_2AgBiBr_6$ can be applied for detectors with high responsivity and detectivity, which are comparable with those of $MAPbX_3$ perovskites.

Wu *et al.* reported an inverted planar heterojunction perovskite solar cell based on $Cs_2AgBiBr_6$ double perovskite with a
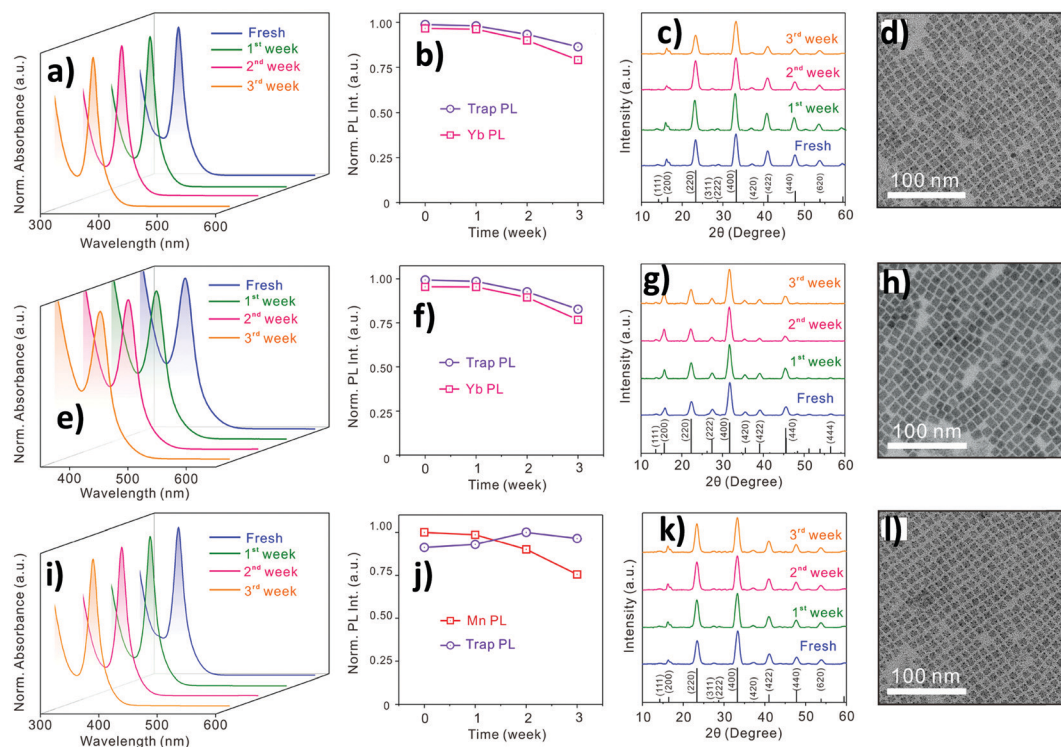

Fig. 17 Stability (optical, structural and morphological) of Yb and Mn doped nanocrystals: (a, e and i) normalized absorption spectra, (b, f and j) normalized PL intensity, (c, g and k) XRD spectra, and (d, h and l) TEM images respectively. Reproduced with permission.[104] Copyright 2019, American Chemical Society.

power conversion efficiency of 2.23%.[91] The authors measured the PL quenching effect of $Cs_2AgBiBr_6$ films on Cu–NiO and C_{60}, which results in prominent decreases of PL intensity, indicating charge transfer from the perovskite film to the charge exciton layers. It was also reported in the literature that the performance of films enhances as the grain size and crystallinity of the films increase with increasing temperature.

A hysteresis-free highest power conversion efficiency of 2.23% is achieved with V_{OC} = 1.01 V, J_{SC} = 3.19 mA cm^{-2}, and FF = 69.2% during the forward scan and a power conversion efficiency of 2.21% results with V_{OC} = 1.00 V, J_{SC} = 3.23 mA cm^{-2}, and FF = 68.4% during the reverse scan (Fig. 18a–d). This value is lower than the theoretical calculation value of 7.92%. This difference may occur for thick double perovskite films.
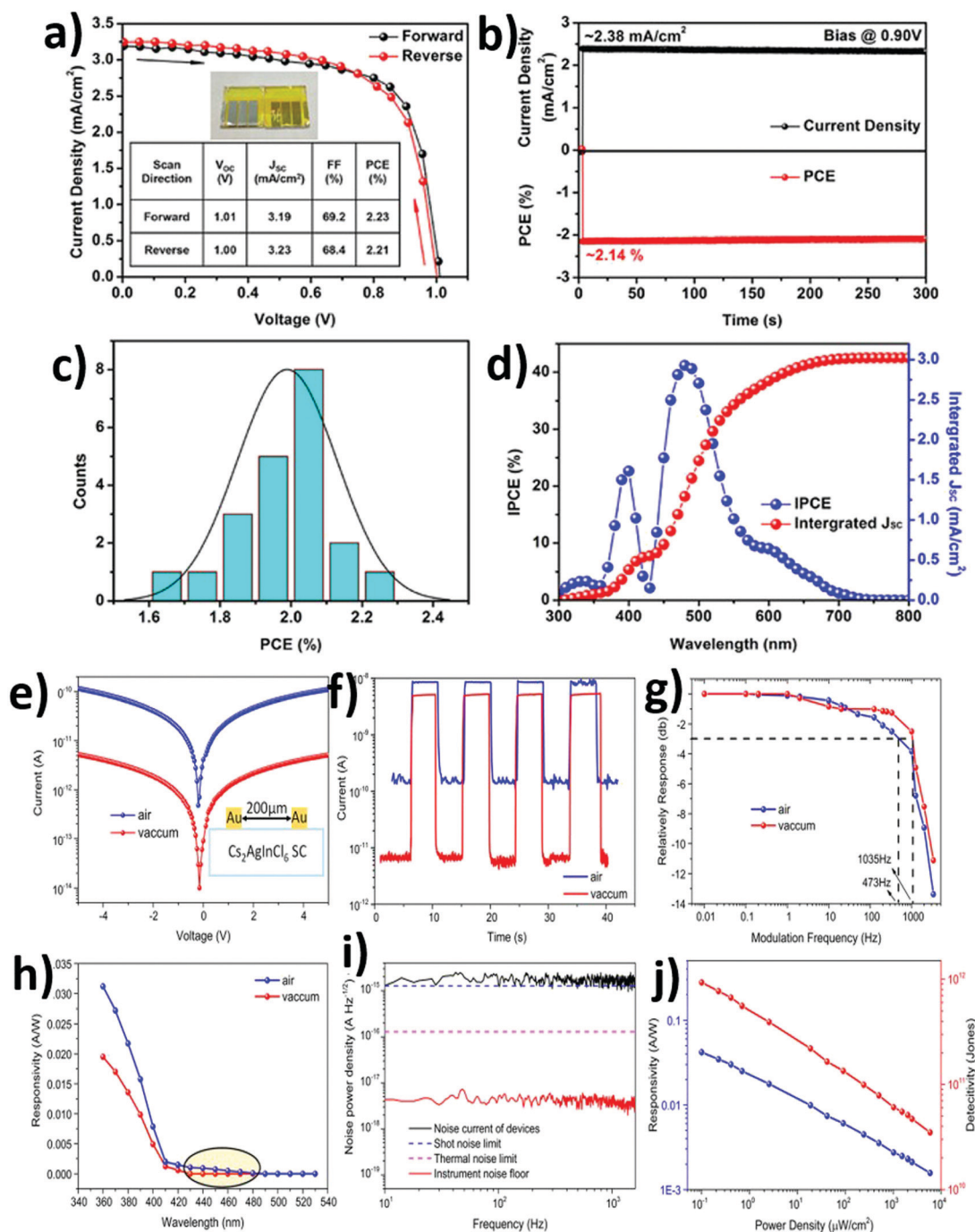
Fig. 18 (a) Forward and reverse scans of J–V curves, (b) stabilized power output together with current density, (c) statistics of the PCE distribution, and (d) IPCE spectra. Reproduced with permission.[91] Copyright 2018, Wiley-VCH. Photoelectric performances of $Cs_2AgInCl_6$ single crystals: (e) current–voltage characteristics under dark conditions, (f) light to dark current voltage curves, (g) normalized response of the detector, (h) wavelength dependent responsivity, (i) measured dark-current noise, and (j) light-intensity dependent responsivity. Reproduced with permission.[105] Copyright 2018, American Chemical Society.

A $Cs_2AgInCl_6$ single crystal was used as a visible-blind UV detector (Fig. 18e–j).[105] The authors performed all the experiments in air and under vacuum to show the effect of oxygen on the device performance. Moreover, $Cs_2AgBiCl_6$ and $Cs_2AgBiBr_6$ have been employed as thermoelectric materials. Use of double perovskites in different aspects has been reported by many groups. Solar energy can be stored in a photochemical cell of the $Cs_2AgBiBr_6$ double perovskite.[106] Here methyl glycogen and cobalt complexes of [cobalt$^{II/III}$tris(bipyridine)] were used and their redox potential was calculated using cyclic voltammetry. At a current density of 0.1 mA cm^{-2}, the charging voltage in the dark was found to be around 1.8 V, which was higher than the potential difference of the coupled cell ($E(MV^+/MV^{2+}) - E(Co^{2+}/Co^{3+})$). This could be due to the higher overpotential required for the conversion of MV^{2+} to MV^+ and Co^{2+} to Co^{3+} or the resistance of ion transfer across the cell membrane. A $Cs_2AgBiBr_6$ thin film can also be used as a photodetector.[107] In order to make the thin film as a photodetector, it was fabricated as a coplanar metal–semiconductor–metal inter-digitated pattern Au electrode configuration. This configuration was like a Au/$Cs_2AgBiBr_6$/Au structure, which facilitated the processes of generation, transfer, and collection of photogenerated carriers. When the energy of the incident light became larger than the semiconductor bandgap, then the film absorbed photons and produced a large number of electron–hole pairs due to the photoelectric effect. These photogenerated carriers rapidly separated and were attracted to the opposite electrode under an external electric field. The photocurrent increases with electric field intensity as the amount of photogenerated carriers is directly proportional to the absorbed photon flux, which follows the law of $I = m \cdot P^{\mu}$, where m is a proportional constant

for a certain wavelength, P is the illumination power of the incident light, and μ represents the response of photocurrent to the given light intensity. The photodetector has higher photo-responsivity, which is measured in terms of the photocurrent generated by the per unit power of incident light for per unit area for a small device area or low light power. Several groups have focused on understanding the nature and working principles of double perovskites on photovoltaic devices. Bartesaghi et al. studied the charge dynamics of $Cs_2AgBiBr_6$ using photo-induced time resolved conductance measurement. The film of the double perovskite exhibited a charge carrier mobility of >1 cm^2 V^{-1} s^{-1}.[108] Pan et al. measured the charge carrier mobility of $Cs_2AgBiBr_6$ single crystals employing a space charge limited current method and the value was 11.81 cm^2 V^{-1} s^{-1}.

Luo et al.[103] reported Na alloyed $Cs_2AgInCl_6$ double perovskite which results in warm white light for indoor lighting.[109] The device was fabricated by pressing the Na alloyed $Cs_2AgInCl_6$ powder into a commercial ultra-violet chip, without any silica encapsulation for protection. The CIE coordinates of the warm white light were (0.396, 0.448) at a colour temperature of 4054 K. There was very negligible degradation for a white LED under operating conditions of 5000 cd m^{-2} for over 1000 h in air, which indicates a promising application for white phosphor.

Single crystals of double perovskites can also be used for X-ray detectors. Yuan et al. synthesized a $Cs_2AgBiBr_6$ single crystal and applied this crystal for the detection of X-rays (Fig. 19).[110] They used phenyl ethylamine bromide which is capable of regulating the order–disorder phase transition into the single crystal and results in the improvement of the ordering extent of alternatively situated $[AgX_6]^{5-}$ and $[BiX_6]^{3-}$ octahedra. By this
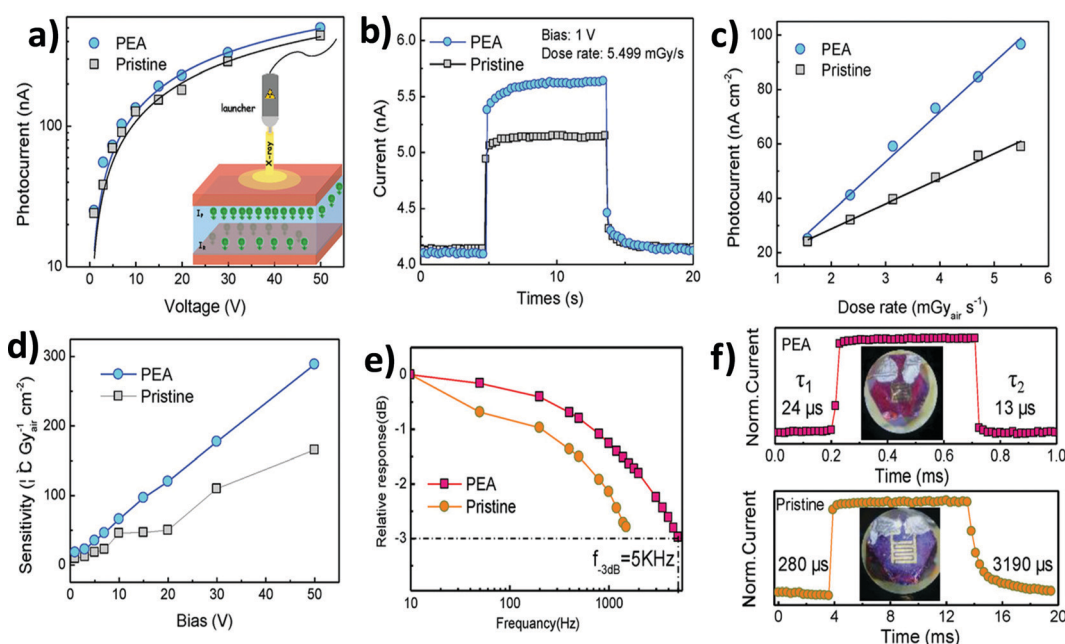
Fig. 19 (a) I–V curves of $Cs_2AgBiBr_6$ and PEA-$Cs_2AgBiBr_6$ single crystal detectors, (b) device response to X-rays, (c) photocurrent intensity as a function of X-ray source, (d) sensitivity under different biases of the X-ray detector, (e) normalized response of the detector to output signal frequency, and (f) photocurrent response of pristine and PEA-$Cs_2AgBiBr_6$ single crystal detectors. Reproduced with permission.[110] Copyright 2019, Wiley-VCH.

process, the defect density and self-trap excitation are suppressed, the band gap is tuned and the carrier mobility is enhanced. Consequently, these make the double perovskite single crystal a potential candidate for X-ray detector application. The photoconductive device made for X-ray detection had an Au/Cs$_2$AgBiBr$_6$/Au structure with an electrode area of 2 mm^2. Photoconductive gain (M) could be calculated by the $M = T_c/T_d$ equation, where T_c represents the carrier lifetime and T_d is the carrier transit time. T_d is equal to $d^2/\mu U$, where d and μ are the carrier transit length and carrier mobility, respectively, and U represents the bias voltage. The authors reported that the μT product values for pristine Cs$_2$AgBiBr$_6$ single crystals and PEA-Cs$_2$AgBiBr$_6$ were 9.14×10^{-4} cm^2 V^{-1} s^{-1} and 1.94×10^{-3} cm^2 V^{-1} s^{-1} respectively. Thus PEA-Cs$_2$AgBiBr$_6$ shows better detection performance compared to the pristine one.

In addition to that, lead-free 2D hybrid halide double perovskites have also been explored for X-ray detection.[111,112] Sun et al. reported (BA)$_2$CsAgBiBr$_7$ and (chloropropylammonium)$_4$AgBiBr$_8$ double perovskites which are highly effective for X-ray detection.[111] The presence of organic cations offers a high mobility lifetime including the low density of traps and defects, and high bulk resistivity, which makes these hybrid lead-free 2D double perovskites promising components for X-ray detection. Simultaneously, iodide a halide-based (4,4-difluoropiperidinium)$_4$AgBiI$_8$ perovskite was studied to investigate its magnetic properties and X-ray detection capacity.[112] Moreover, a lead-free 2D hybrid double perovskite was reported as strong polarization sensitive materials.[113] The alteration of organic–inorganic sheets in (i-PA)$_2$CsAgBiBr$_7$ results in a quantum-confined bilayered structure of 2D archetype which shows high anisotropy in terms of physical properties that include optical absorption and electrical properties. This anisotropic nature of the 2D hybrid double perovskite results in a strong polarization-sensitive response.

Weng et al. reported a Cs$_2$AgBiBr$_6$ perovskite microcrystal as a humidity sensor and it was operated in the humidity range of 15% to 78% at 25 °C.[114] The device was prepared by the anti-solvent drop casting method on a silica substrate where the precursor halides were dissolved in DMSO, and methyl benzene was used as an anti-solvent.

The response and recovery times of the Cs$_2$AgBiBr$_6$ thin film were 1.78 and 0.45 s respectively. The high recovery time of the thin film results from the plane structure of the film, from where water molecules can be easily volatilized during the desorption process.

Zhou et al. reported photocatalytic CO$_2$ reduction by Cs$_2$AgBiBr$_6$ perovskite nanocrystals where the electron consumption was 105 μmol g^{-1} under AM 1.5G illumination for 6 h (Fig. 20).[103] Upon constant irradiation for 6 hours the unwashed nanocrystal is able to evaluate CO (R(CO)) and CH$_4$ (R(CH$_4$)) with the quantity of 5.5 and 0.65 μmol g^{-1} respectively without any H$_2$ evolution. The ethanol washed nanocrystal evaluate R(CO) and R(CH$_4$) with the quantity of 14.1 and 9.6 μmol g^{-1} respectively which is 6.5 fold more than the unwashed nanocrystals. In this contrast, Xu et al. reported successful application of Cs$_2$AgBiBr$_6$ nanocrystals for photocatalytic dye degradation for Rhodamine B (RhB), Rhodamine
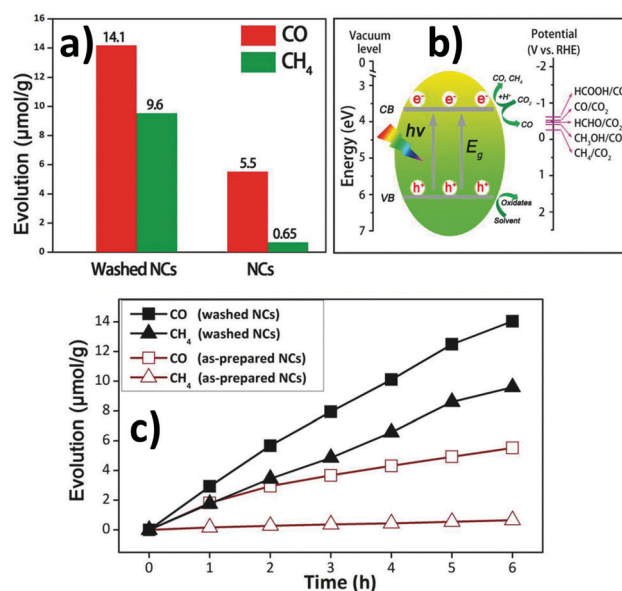
Fig. 20 (a) Comparison of the performance of CO$_2$ reduction between the as-prepared and washed Cs$_2$AgBiBr$_6$ nanocrystals, (b) photo-reduction of CO$_2$ on the surfaces of the nanocrystals, and (c) time courses of CO and CH$_4$ evolution. Reproduced with permission.[103] Copyright 2018, Wiley-VCH.

110 (Rh110), methyl red (MR), and methyl orange (MO) under visible-light irradiation ($\lambda > 420$ nm).[115] In the case of Rhodamine B dye, the degradation process needs 12 hours for completion. The overall photodegradation process goes through the superoxide radical reaction and follows zeroth order kinetics. Other dyes degrade very slowly as compared to Rhodamine B dye because the surface of RhB is negatively charged, which facilitates the adsorption of positive charged RhB dye more effectively in comparison with neutral or anionic molecules like MO and MR.

7. Limitations of double perovskites

Lead-free halide double perovskites have attracted excellent research attention due to their high stability and tunable absorption-emission in the whole UV and visible regions. In this contrast, double perovskites have some limitations for which they experience a few obstacles for a large scale commercial application in the field of optoelectronic devices. Now we will discuss these factors.

A. One of the most important drawbacks of double perovskites is their low photoluminescence quantum yields. Several groups have focused on increasing the PLQY of double perovskites. Sometimes doping with another metal ion or adding water during synthesis may result in an increase in the PLQY of double perovskites to some extent by suppressing the surface defect.

B. Usually double perovskites have a stable cubic structure. However, the cubic unit cell sometimes restricts the orbital interaction which leads to a narrow conduction band and a large bandgap.

C. Preparation of double perovskites needs high temperature which causes difficulty to some extent in device fabrication.

D. Usually, PL spectra of double perovskites are broad in nature which consist of large FWHM values. Therefore, it is difficult to obtain color purity in the CIE coordinates.

E. In order to understand the charge transfer process, charge carrier dynamics should be investigated more deeply.

F. Dimensional reduction of double perovskites may help in overcoming the problems of electronic structures and results in bandgap transition.

G. The morphology (size and shape) of halide perovskites could be tuned easily.It is difficult to tune the morphology of double perovskite easily.

H. We have to precisely control the amounts of starting materials during the formation of double perovskites. In addition to that, component engineering could be possible by doping with rare earth elements, which may cause a significant change in optical properties.

In spite of all the obstacles, double perovskites have gained considerable research interest recently and have established themselves as promising alternatives to lead halide perovskites. Beyond solar cell application, double perovskites can be successfully implemented in sensors, photocatalysis, LEDs, photodetectors, X-ray detectors, etc.

8. Summary and outlook of the review

In this review, we have gone through a complete survey of double perovskite microcrystals and nanocrystals. Here, we have discussed how double perovskites can be synthesized in a variety of ways. This review has demonstrated that, depending on the methodology of reaction processes, the optical properties of double perovskites change, which is established by several photo-physical techniques. It has been noticed through morphological evolution that double perovskites have different shapes in nano- as well as microphases. Double perovskites have gained importance over lead based perovskites due to their high stability. We have explained different factors responsible for the high stability of double perovskites. Moreover, different applications of double perovskites have been vastly explored here. Simultaneously, all the merits and demerits of double perovskites have been discussed here. Therefore, we hope that this review will present a clear understanding about various properties of double perovskites and attract a broad readership.

Conflicts of interest

The authors declare no conflict of interest.

Acknowledgements

References

1 Z. A. Borgschulte and L. Sachlapbach, *Hydrogen as a Future Energy Carrier*, Wiley-VCH Verlag GmbH & Co., 2008, ISBN: 978-3-527-30817-0.

2 J. R. Petit, *Nature*, 1999, **399**, 429–436.

3 P. M. Vignais and B. Billoud, *Chem. Rev.*, 2007, **107**, 4206–4272.

4 V. Artero and M. Fontecave, *Coord. Chem. Rev.*, 2005, **249**, 1518–1535.

5 J. F. Capon, F. Gloaguen, P. Schollhammer and J. Talarmin, *Coord. Chem. Rev.*, 2005, **249**, 1664–1676.

6 M. C. Weidman, A. J. Goodman and W. A. Tisdale, *Chem. Mater.*, 2017, **29**, 5019–5030.

7 C. K. Moller, *Nature*, 1958, **182**, 1436.

8 J. Wang, J. Dong, F. Lu, C. Sun, Q. Zhang and N. Wang, *J. Mater. Chem. A*, 2019, **7**, 23563–23576.

9 S. Demic, A. N. Ozcivan, M. Can, C. Ozbek and M. Karakaya, Recent Progresses in Perovskite Solar Cells, in *Nanostructured Solar Cells*, Intech, Rijeka, Croatia, 2017, pp. 277–304.

10 A. Kojima, K. Teshima, Y. Shirai and T. Miyasaka, *J. Am. Chem. Soc.*, 2009, **131**, 6050–6051.

11 (a) Z. G. Xiao, R. A. Kerner, L. F. Zhao, N. L. Tran, K. M. Lee, T. W. Koh, G. D. Scholes and B. P. Rand, *Nat. Photonics*, 2017, **11**, 108–115; (b) T. Chen, Y. Xu, Z. Xie, W. Jiang, L. Wang and W. Jiang, *Nanoscale*, 2020, **12**, 9569–9580.

12 I. L. Braly, D. W. deQuilettes, L. M. Pazos-Outón, S. Berke, M. E. Ziffer, D. S. Ginger and H. W. Hillhouse, *Nat. Photonics*, 2018, **12**, 355–361.

13 (a) P. Bansal, Y. Khan and P. Kar, *Chem. Commun.*, 2018, **54**, 3508–3511; (b) P. Bansal and P. Kar, *Chem. Commun.*, 2019, **55**, 6543–6546; (c) P. Bansal, Y. Khan and P. Kar, *New J. Chem.*, 2019, **43**, 4116–4122; (d) A. K. Sharma, P. Bansal, G. K. Nim and P. Kar, *Part. Part. Syst. Charact.*, 2019, **36**, 1900328; (e) H. Shankar, P. Bansal, W. W. Yu and P. Kar, *Chem. – Eur. J.*, 2020, **26**, 12242–12248.

14 J. F. Liao, W. Q. Wu, J. X. Zhong, Y. Jiang, L. Wang and D. B. Kuang, *J. Mater. Chem. A*, 2019, **7**, 9025–9033.

15 J. Qian, B. Xu and W. Tian, *Org. Electron.*, 2016, **37**, 61–73.

16 W. Travis, E. N. K. Glover, H. Bronstein, D. O. Scanlon and R. G. Palgrave, *Chem. Sci.*, 2016, **7**, 4548–4556.

17 T. J. Huang, Z. X. Thiang, X. Yin, C. Tang, G. Qi and H. Gong, *Chem. – Eur. J.*, 2016, **22**, 2146–2152.

18 V. M. Goldschmidt, *Naturwissenschaften*, 1926, **14**, 477–485.

19 C. Li, X. Lu, W. Ding, L. Feng, Y. Gao and Z. Guo, *Acta Crystallogr., Sect. B: Struct. Sci.*, 2008, **64**, 702–707.

20 G. K. Nim, P. Bansal and P. Kar, *ACS Omega*, 2019, **4**, 15678–15683.

21 M. Johnsson and P. Lemmens, Crystallography and chemistry of perovskites, in *Handbook of magnetism and advanced magnetic materials*, Wiley Online Library, 2007, DOI: **10.1002/9780470022184.hmm411**.

22 J. I. Uribe, D. Ramirez, J. M. Osorio-Guillén, J. Osorio and F. Jaramillo, *J. Phys. Chem. C*, 2016, **120**, 16393–16398.

23 G. Kieslich, S. Sun and A. K. Cheetham, *Chem. Sci.*, 2014, **5**, 4712–4715.

24 W. S. Yang, B. W. Park, E. H. Jung, N. J. Jeon, Y. C. Kim, D. U. Lee, S. S. Shin, J. Seo, E. K. Kim, J. H. Noh and S. Seok, *Science*, 2017, **356**, 1376–1379.

25 T. Fang, T. Wang, X. Li, Y. Dong, S. Bai and J. Song, *Sci. Bull.*, 2021, **66**, 36–43.

26 (*a*) Q. Li, L. Zhang, Z. Chen and Z. Quan, *J. Mater. Chem. A*, 2019, **7**, 16089–16108; (*b*) Y. Dong, X. Tang, Z. Zhang, J. Song, T. Niu, D. Shan and H. Zeng, *Matter*, 2020, **3**, 273–286; (*c*) X. Liu, Z. Wu, T. Guan, H. Jiang, P. Long, X. Li, C. Ji, S. Chen, Z. Sun and J. Luo, *Nat. Commun.*, 2021, **12**, 5502; (*d*) Y. Ma, J. Wang, W. Guo, S. Han, J. Xu, Y. Liu, L. Lu, Z. Xie, J. Luo and Z. Sun, *Adv. Funct. Mater.*, 2021, **31**, 2103012.

27 (*a*) K. B. Lin, J. Xing, L. N. Quan, F. Pelayo, G. de Arquer, X. Gong, J. Lu, L. Xie, W. Zhao, D. Zhang, C. Yan, W. Li, X. Liu, Y. Lu, J. Kirman, E. H. Sargent, Q. Xiong and Z. Wei, *Nature*, 2018, **562**, 245–248; (*b*) R. Sun, P. Lu, D. Zhou, W. Xu, N. Ding, H. Shao, Y. Zhang, D. Li, N. Wang, X. Zhuang, B. Dong, H. Song and X. Bai, *ACS Energy Lett.*, 2020, **5**, 2131–2139; (*c*) L. Xu, J. Li, B. Cai, J. Song, F. Zhang, T. Fang and H. Zeng, *Nat. Commun.*, 2020, **11**, 3902.

28 (*a*) Y. Huang, T. Liu, C. Liang, J. Xia, D. Li, H. Zhang, A. Amini, G. Xing and C. Cheng, *Adv. Funct. Mater.*, 2020, **30**, 2000863; (*b*) M. H. Li, S. C. Liu, F. Z. Qiu, Z. Y. Zhang, D. J. Xue and J. S. Hu, *Adv. Energy Mater.*, 2020, **10**, 2000501.

29 (*a*) H. Zhou, J. Zeng, Z. Song, C. R. Grice, C. Chen, Z. Song, D. Zhao, H. Wang and Y. Yan, *J. Phys. Chem. Lett.*, 2018, **9**, 2043–2048; (*b*) L. Xuhai, Y. Dejian, C. Fei, L. Xiaoming, J. Jianping, C. Jun, S. Xiufeng and Z. Haibo, *Small*, 2017, **13**, 1700364.

30 X. S. Tang, Z. P. Hu, W. Yuan, W. Hu, H. Shao, D. Han, J. Zheng, J. Hao, Z. Zang, J. Du, Y. Leng, L. Fang and M. Zhou, *Adv. Opt. Mater.*, 2017, **5**, 1600788.

31 X. Y. Chin, D. Cortecchia, J. Yin, A. Bruno and C. Soci, *Nat. Commun.*, 2015, **6**, 7383.

32 X. S. Tang, S. Han, Z. Q. Zu, W. Hu, D. Zhou, J. Du, Z. Hu, S. Li and Z. Zang, *Front. Phys.*, 2018, **5**, 69.

33 C. Zhang, B. Wang, W. Li, S. Huang, L. Kong, Z. Li and L. Li, *Nat. Commun.*, 2017, **8**, 1138.

34 (*a*) X. Liu, J. Gao, W. Liu and Q. Wang, *J. Alloys Compd.*, 2020, **817**, 152693; (*b*) B. Conings, J. Drijkoningen, N. Gauquelin, A. Babayigit, J. D'Haen, L. D'Olieslaeger, A. Ethirajan, J. Verbeeck, J. Manca, E. Mosconi, F. D. Angelis and H.-G. Boyen, *Adv. Energy Mater.*, 2015, **5**, 1500477.

35 N. A. Manshor, Q. Wali, K. K. Wong, S. K. Muzakir, A. Fakharuddin, L. Schmidt-Mende and R. Jose, *Phys. Chem. Chem. Phys.*, 2016, **18**, 21629–21639.

36 G. Niu, X. Guo and L. Wanga, *J. Mater. Chem. A*, 2015, **3**, 8970–8980.

37 J. A. Christians, P. A. Miranda Herrera and P. V. Kamat, *J. Am. Chem. Soc.*, 2015, **137**, 1530–1538.

38 J. H. Noh, S. H. Im, J. H. Heo, T. N. Mandal and S. Seok, *Nano Lett.*, 2013, **13**, 1764–1769.

39 Y. Zhang, M. I. Saidaminov, I. Dursun, H. Yang, B. Murali, E. Alarousu, E. Yengel, B. A. Alshankiti, O. M. Bakr and O. F. Mohammed, *J. Phys. Chem. Lett.*, 2017, **8**, 961–965.

40 (*a*) Q. Zhang, F. Hao, J. Li, Y. Zhou, Y. Wei and H. Lin, *Sci. Technol. Adv. Mater.*, 2018, **19**, 425–442; (*b*) H. Needleman, *Annu. Rev. Med.*, 2004, **55**, 209–222.

41 J. Bressler, K.-a. Kim, T. Chakraborti and G. Goldstein, *Neurochem. Res.*, 1999, **24**, 595–600.

42 P.-C. Hsu and Y. L. Guo, *Toxicology*, 2002, **180**, 33–44.

43 H. L. Clever and F. J. Johnston, *J. Phys. Chem. Ref. Data*, 1980, **9**, 751–784.

44 A. H. Slavney, R. W. Smaha, I. C. Smith, A. Jaffe, D. Umeyama and H. I. Karunadasa, *Inorg. Chem.*, 2017, **56**, 46–55.

45 K. I. Kobayashi, T. Kimura, H. Sawada, K. Terakura and Y. Tokura, *Nature*, 1998, **395**, 677–680.

46 S. Sengodan, S. Choi, A. Jun, T. H. Shin, Y.-W. Ju, H. Y. Jeong, J. Shin, J. T. S. Irvine and G. Kim, *Nat. Mater.*, 2014, **14**, 205–209.

47 Y. Liu, Z. Wang, J.-P. M. Veder, Z. Xu, Y. Zhong, W. Zhou, M. O. Tade, S. Wang and Z. Shao, *Adv. Energy Mater.*, 2018, **8**, 1702604.

48 S. Yoo, A. Jun, Y.-W. Ju, D. Odkhuu, J. Hyodo, H. Y. Jeong, N. Park, J. Shin, T. Ishihara and G. Kim, *Angew. Chem., Int. Ed.*, 2014, **53**, 13064–13067.

49 R. N. Mahato, K. Sethupathi and V. Sankaranarayanan, *J. Appl. Phys.*, 2010, **107**, 09D714.

50 J.-W. G. Bos, J. P. Attfield and Z. Anorg, *Allg. Chem.*, 2004, **630**, 2248–2252.

51 Y. Moritomo, S. Xu, A. Machida, T. Akimoto, E. Nishibori, M. Takata, M. Sakata and K. Ohoyama, *J. Phys. Soc. Jpn.*, 2000, **69**, 1723–1726.

52 D. D. Sarma, E. V. Sampathkumaran, S. Ray, R. Nagarajan, S. Majumdar, A. Kumar, G. Nalini and T. N. Guru Row, *Solid State Commun.*, 2000, **114**, 465–468.

53 R. D. Shannon, *Acta Crystallogr., Sect. A: Cryst. Phys., Diffr., Theor. Gen. Crystallogr.*, 1976, **32**, 751–767.

54 Q. Chen, N. De Marco, Y. Yang, T.-B. Song, C.-C. Chen, H. Zhao, Z. Hong, H. Zhou and Y. Yang, *Nano Today*, 2015, **10**, 355–396.

55 B. Saparov and D. Mitzi, *Chem. Rev.*, 2016, **116**, 4558–4596.

56 (*a*) A. Jha, P. Bansal, G. K. Nim and P. Kar, *Opt. Mater.*, 2021, **111**, 110660; (*b*) J. Huang, T. Lei, M. Siron, Y. Zhang, S. Yu, F. Seeler, A. Dehestani, L. N. Quan, K. Schierle-Arndt and P. Yang, *Nano Lett.*, 2020, **20**, 3734–3739.

57 N. K. Noel, S. D. Stranks, A. Abate, C. Wehrenfennig, S. Guarnera, A.-A. Haghighirad, A. Sadhanala, G. E. Eperon, S. K. Pathak, M. B. Johnston, A. Petrozza, L. M. Herz and H. J. Snaith, *Energy Environ. Sci.*, 2014, **7**, 3061–3068.

58 M. R. Filip and F. Giustino, *J. Phys. Chem. C*, 2016, **120**, 166–173.

59 H. Shankar, S. Ghosh and P. Kar, *J. Alloys Compd.*, 2020, **844**, 156148.

60 (*a*) Z. Tan, Y. Chu, J. Chen, J. Li, G. Ji, G. Niu, L. Gao, Z. Xiao and J. Tang, *Adv. Mater.*, 2020, **32**, 2002443;

(b) A. Karmakar, S. Mukhopadhyay, P. G. B. Gachod, V. A. Mora-Gomez, G. M. Bernard, A. Brown and V. K. Michaelis, *Chem. Mater.*, 2021, **33**, 6078–6090; (c) Z. Xiao, W. Meng, J. Wang and Y. Yan, *ChemSusChem*, 2016, **9**, 2628–2633; (d) A. Noculak, V. Morad, K. M. McCall, S. Yakunin, Y. Shynkarenko, M. Wörle and M. V. Kovalenko, *Chem. Mater.*, 2020, **32**, 5118–5124; (e) A. Karmakar, G. M. Bernard, A. Meldrum, A. O. Oliynyk and V. K. Michaelis, *J. Am. Chem. Soc.*, 2020, **142**, 10780–10793; (f) C.-Y. Wang, P. Liang, R.-J. Xie, Y. Yao, P. Liu, Y. Yang, J. Hu, L. Shao, X. W. Sun, F. Kang and G. Wei, *Chem. Mater.*, 2020, **32**, 7814–7821; (g) S. Ghosh, G. K. Nim, H. Shankar and P. Kar, *New J. Chem.*, 2021, **45**, 22691–22696.

61 A. Jain, O. Voznyy and E. H. Sargent, *J. Phys. Chem. C*, 2017, **121**, 7183–7187.

62 F. Igbari, Z.-K. Wang and L.-S. Liao, *Adv. Mater.*, 2018, 1802697.

63 M. Roknuzzaman, C. Zhang1, K. (Ken) Ostrikov, A. Du, H. Wang, L. Wang and T. Tesfamichae, *Sci. Rep.*, 2019, **9**, 718.

64 (a) A. Fakharuddin, U. Shabbir, W. Qiu, T. Iqbal, M. Sultan, P. Heremans and L. Chmidt-Mende, *Adv. Mater.*, 2019, 1807095; (b) G. Longo, S. Mahesh, L. R. Buizza, A. D. Wright, A. J. Ramadan, M. Abdi-Jalebi, P. K. Nayak, L. M. Herz and H. J. Snaith, *ACS Energy Lett.*, 2020, **5**, 2200–2207; (c) J. Euvrard, X. Wang, T. Li, Y. Yan and D. B. Mitzi, *J. Mater. Chem. A*, 2020, **8**, 4049–4054; (d) W. Lin, G. Chen, E. Li, L. He, W. Yu, G. Peng, H. Chen and T. Guo, *ACS Appl. Mater. Interfaces*, 2020, **12**, 43967–43975; (e) X. Wang, K. Li, H. Xu, N. Ali, Y. Wang, Q. Shen and H. Wu, *Chem. Commun.*, 2020, **56**, 7917–7920; (f) T. Wang, D. Yue, X. Li and Y. Zhao, *Appl. Catal., B*, 2020, **268**, 118399.

65 V. K. Ravi, N. Singhal and A. Nag, *J. Mater. Chem. A*, 2018, **6**, 21666–21675.

66 Z. Xiao, Z. Song and Y. Yan, *Adv. Mater.*, 2019, **31**, 1803792.

67 Q. Fan, G. V. Biesold McGee, Q. Xu, S. Pan, J. Peng, J. Ma and Z. Lin, *Angew. Chem.*, 2020, **59**, 1030–1046.

68 F. Wei, Z. Deng, S. Sun, F. Xie, G. Kieslich, D. M. Evans, M. A. Carpenter, P. D. Bristowea and A. K. Cheetham, *Mater. Horiz.*, 2016, **3**, 328–332.

69 F. Wei, Z. Deng, S. Sun, F. Zhang, D. M. Evans, G. Kieslich, S. Tominaka, M. A. Carpenter, J. Zhang, P. D. Bristowe and A. K. Cheetham, *Chem. Mater.*, 2017, **29**, 1089–1094.

70 Z. Deng, F. Wei, S. Sun, G. Kieslich, A. K. Cheetham and P. D. Bristowe, *J. Mater. Chem. A*, 2016, **4**, 12025–12029.

71 Q. Sun, H. Chen and W.-J. Yin, *Chem. Mater.*, 2019, **31**, 244–250.

72 A. H. Slavney, T. Hu, A. M. Lindenberg and H. I. Karunadasa, *J. Am. Chem. Soc.*, 2016, **138**, 2138–2141.

73 L.-Z. Lei, Z.-F. Shi, Y. Li, Z.-Z. Ma, F. Zhang, T.-T. Xu, Y.-T. Tian, D. Wu, X.-J. Lia and G.-T. Du, *J. Mater. Chem. C*, 2018, **6**, 7982–7988.

74 G. Volonakis, M. R. Filip, A. A. Haghighirad, N. Sakai, B. Wenger, H. J. Snaith and F. Giustino, *J. Phys. Chem. Lett.*, 2016, **7**, 1254–1259.

75 E. T. McClure, M. R. Ball, W. Windl and P. M. Woodward, *Chem. Mater.*, 2016, **28**, 1348–1354.

76 S. Ghosh, G. K. Nim, P. Bansal and P. Kar, *J. Colloid Interface Sci.*, 2021, **582**, 1223–1230.

77 Y. Mahor, W. J. Mir and A. Nag, *J. Phys. Chem. C*, 2019, **123**, 15787–15793.

78 N. K. Nandha and A. Nag, *Chem. Commun.*, 2018, **54**, 5205–5208.

79 J. Zhou, Z. Xia, M. S. Molokeev, X. Zhang, D. Peng and Q. Liu, *J. Mater. Chem. A*, 2017, **5**, 15031–15037.

80 (a) A. Karmakar, M. S. Dodd, S. Agnihotri, E. Ravera and V. K. Michaelis, *Chem. Mater.*, 2018, **30**, 8280–8290; (b) Q. Liao, J. Chen, L. Zhou, T. Wei, L. Zhang, D. Chen, F. Huang, Q. Pang and J. Z. Zhang, *J. Phys. Chem. Lett.*, 2020, **11**, 8392–8398.

81 G. Volonakis, A. A. Haghighirad, R. L. Milot, W. H. Sio, M. R. Filip, B. Wenger, M. B. Johnston, L. M. Herz, H. J. Snaith and F. Giustino, *J. Phys. Chem. Lett.*, 2017, **8**, 772–778.

82 B. Yang, J. Chen, S. Yang, F. Hong, L. Sun, P. Han, T. Pullerits, W. Deng and K. Han, *Angew. Chem., Int. Ed.*, 2018, **57**, 5359–5363.

83 J. C. Dahl, W. T. Osowiecki, Y. Cai, J. K. Swabeck, Y. Bekenstein, M. Asta, E. M. Chan and A. P. Alivisatos, *Chem. Mater.*, 2019, **31**, 3134–3143.

84 F. Locardi, M. Cirignano, D. Baranov, Z. Dang, M. Prato, F. Drago, M. Ferretti, V. Pinchetti, M. Fanciulli, S. Brovelli, L. De Trizio and L. Manna, *J. Am. Chem. Soc.*, 2018, **140**, 12989–12995.

85 P. Han, X. Zhang, C. Luo, W. Zhou, S. Yang, J. Zhao, W. Deng and K. Han, *ACS Cent. Sci.*, 2020, **6**, 566–572.

86 S. E. Creutz, E. N. Crites, M. C. De Siena and D. R. Gamelin, *Nano Lett.*, 2018, **18**, 1118–1123.

87 D. Manna, T. K. Das and A. Yella, *Chem. Mater.*, 2019, **31**, 10063–10070.

88 T. Umebayashi, K. Asai, T. Kondo and A. Nakao, *Phys. Rev. B: Condens. Matter Mater. Phys.*, 2003, **67**, 155405.

89 (a) W.-J. Yin, J.-H. Yang, J. Kang, Y. Yan and S.-H. Wei, *J. Mater. Chem. A*, 2015, **3**, 8926–8942; (b) M. H. Du, *J. Mater. Chem. A*, 2014, **2**, 9091–9098; (c) E. Greul, M. L. Petrus, A. Binek, P. Docampo and T. Bein, *J. Mater. Chem. A*, 2017, **5**, 19972–19981.

90 T. T. Tran, J. R. Panella, J. R. Chamorro, J. R. Morey and T. M. McQueen, *Mater. Horiz.*, 2017, **4**, 688–693.

91 W. Gao, C. Ran, J. Xi, B. Jiao, W. Zhang, M. Wu, X. Hou and Z. Wu, *ChemPhysChem*, 2018, **19**, 1690–1700.

92 X. Zhao, J. Yang, Y. Fu, D. Yang, Q. Xu, L. Yu, S.-H. Wei and L. Zhang, *J. Am. Chem. Soc.*, 2017, **139**, 2630–2638.

93 X.-G. Zhao, D. Yang, Y. Sun, T. Li, L. Zhang, L. Yu and A. Zunger, *J. Am. Chem. Soc.*, 2017, **139**, 6718–6725.

94 J. Zhou, X. Rong, M. S. Molokeev, X. Zhang and Z. Xia, *J. Mater. Chem. A*, 2018, **6**, 2346–2352.

95 C. N. Savory, A. Walsh and D. O. Scanlon, *ACS Energy Lett.*, 2016, **1**, 949–955.

96 S. Wang, Y. Jiang, E. J. Juarez-Perez, L. K. Ono and Y. Qi, *Nat. Energy*, 2017, **2**, 16195.

97 A. H. Slavney, L. Leppert, D. Bartesaghi, A. Gold-Parker, M. F. Toney, T. J. Savenije, J. B. Neaton and H. I. Karunadasa, *J. Am. Chem. Soc.*, 2017, **139**, 5015–5018.

98 W. Ning, F. Wang, B. Wu, J. Lu, Z. Yan, X. Liu, Y. Tao, J.-M. Liu, W. Huang, M. Fahlman, L. Hultman, T. C. Sum and F. Gao, *Adv. Mater.*, 2018, **30**, 1706246.

99 C. Wu, Q. Zhang, Y. Liu, W. Luo, X. Guo, Z. Huang, H. Ting, W. Sun, X. Zhong, S. Wei, S. Wang, Z. Chen and L. Xiao, *Adv. Sci.*, 2018, **5**, 1700759.

100 W. Pan, H. Wu, J. Luo, Z. Deng, C. Ge, C. Chen, X. Jiang, W.-J. Yin, G. Niu, L. Zhu, L. Yin, Y. Zhou, Q. Xie, X. Ke, M. Sui and J. Tang, *Nat. Photonics*, 2017, **11**, 726–732.

101 Y. Bekenstein, B. A. Koscher, S. W. Eaton, P. Yang and A. P. Alivisatos, *J. Am. Chem. Soc.*, 2015, **137**, 16008–16011.

102 J. De Roo, M. Ibanez, P. Geiregat, G. Nedelcu, W. Walravens, J. Maes, J. C. Martins, I. Van Driessche, M. V. Kovalenko and Z. Hens, *ACS Nano*, 2016, **10**, 2071–2081.

103 L. Zhou, Y.-F. Xu, B.-X. Chen, D.-B. Kuang and C.-Y. Su, *Small*, 2018, **14**, 1703762.

104 N. Chen, T. Cai, W. Li, K. Hills-Kimball, H. Yang, M. Que, Y. Nagaoka, Z. Liu, D. Yang, A. Dong, C.-Y. Xu, R. Zia and O. Chen, *ACS Appl. Mater. Interfaces*, 2019, **11**, 16855–16863.

105 J. Luo, S. Li, H. Wu, Y. Zhou, Y. Li, J. Liu, J. Li, K. Li, F. Yi, G. Niu and J. Tang, *ACS Photonics*, 2018, **5**, 398–405.

106 K. Prabhu and A. K. Chandiran, *Chem. Commun.*, 2020, **56**, 7329–7332.

107 L.-Z. Lei, Z.-F. Shi, Y. Li, Z.-Z. Ma, F. Zhang, T.-T. Xu, Y.-T. Tian, D. Wu, X.-J. Lia and G.-T. Dub, *J. Mater. Chem. C*, 2018, **6**, 7982–7988.

108 D. Bartesaghi, A. H. Slavney, M. C. Gelvez-Rueda, B. A. Connor, F. C. Grozema, H. I. Karunadasa and T. J. Savenije, *J. Phys. Chem. C*, 2018, **122**, 4809–4816.

109 J. Luo, X. Wang, S. Li, J. Liu, Y. Guo, G. Niu, L. Yao, Y. Fu, L. Gao, Q. Dong, C. Zhao, M. Leng, F. Ma, W. Liang, L. Wang, S. Jin, J. Han, L. Zhang, J. Etheridge, J. Wang, Y. Yan, E. H. Sargent and J. Tang, *Nature*, 2018, **563**, 541–545.

110 W. Yuan, G. Niu, Y. Xian, H. Wu, H. Wang, H. Yin, P. Liu, W. Li and J. Fan, *Adv. Funct. Mater.*, 2019, **29**, 1900234.

111 (*a*) Z. Xu, X. Liu, Y. Li, X. Liu, T. Yang, C. Ji, S. Han, Y. Xu, J. Luo and Z. Sun, *Angew. Chem., Int. Ed.*, 2019, **58**, 15757–15761; (*b*) W. Guo, X. Liu, S. Han, Y. Liu, Z. Xu, M. Hong, J. Luo and Z. Sun, *Angew. Chem., Int. Ed.*, 2020, **59**, 13879–13884.

112 C.-F. Wang, H. Li, M.-G. Li, Y. Cui, X. Song, Q.-W. Wang, J.-Y. Jiang, M.-M. Hua, Q. Xu, K. Zhao, H.-Y. Ye and Y. Zhang, *Adv. Funct. Mater.*, 2021, **31**, 2009457.

113 Y. Li, T. Yang, Z. Xu, X. Liu, X. Huang, S. Han, Y. Liu, M. Li, J. Luo and Z. Sun, *Angew. Chem., Int. Ed.*, 2020, **59**, 3429–3433.

114 Z. Weng, J. Qin, A. A. Umar, J. Wang, X. Zhang, H. Wang, X. Cui, X. Li, L. Zheng and Y. Zhan, *Adv. Funct. Mater.*, 2019, **29**, 1902234.

115 Z. Zhang, Y. Liang, H. Huang, X. Liu, Q. Li, L. Chen and D. Xu, *Angew. Chem.*, 2019, **58**, 7263–7267.